Optimality criteria-based minimum-weight design method for modular building systems subjected to generalised stiffness constraints: a comparative study

[1]Zixiao Wang and [2]Konstantinos Daniel Tsavdaridis

[1]Post-doctoral Fellow, School of Civil Engineering, Faculty of Engineering and Physical Sciences, University of Leeds, Woodhouse Lane, LS2 9JT, Leeds, UK

[2]Associate Professor of Structural Engineering, School of Civil Engineering, Faculty of Engineering and Physical Sciences, University of Leeds, Woodhouse Lane, LS2 9JT, Leeds, UK

(k.tsavdaridis@leeds.ac.uk)

ABSTRACT

Recently, modular construction and prefabrication have gained massive momentum as they continue to help many cities around the globe to tackle the ongoing housing crisis and to meet the pressing demands for healthcare facilities during the coronavirus pandemic. Previous studies focused only on employing optimisation techniques at the member level to enhance the structural capacity of steel beams in modular building systems (MBS). This paper explores the feasibility and efficacy of an optimality criteria (OC)-based minimum-weight design method in reducing self-weights of MBS while maintaining their overall lateral stiffness measured by natural/resonant frequency. This is pursued through an innovative optimisation investigation involving a three-storey, self-standing MBS with hinged inter-module joints, together with a comparative moment-resisting frame (MRF) benchmark structure with two different beam-column connection rigidities. Continuous-valued sizing optimisation of two structural systems under a single frequency constraint is achieved through a novel, numerically stable, iterative algorithm. The latter is developed from a frequency-related OC formulated rigorously through the Lagrangian multiplier approach. The discrete minimum-weight design is facilitated by a mapping strategy designed to round the continuous optimum to the nearest, most economical standard steel sections. It is found that the proposed minimum-weight design method can achieve significant steel savings for the adopted MBS without compromising its lateral stiffness. Further, it is shown that the MRF structure with

semi-rigid connections can meet the same frequency constraints with slightly smaller steel tonnages. It is envisioned that this study will pave the way towards achieving resilient and cost-effective modular units and tall MBS that further support the building industry in meeting its goals of efficiency and sustainability.

Keywords: modular building systems; sizing optimisation; minimum-weight design; optimality criteria

1. INTRODUCTION

In recent years, rapid urbanisation trends have created pressing demands for affordable residential and office space in many major cities around the globe, thereby urging the construction industry to adapt towards more innovative engineering solutions and construction methods. Meanwhile, buildings and construction are now responsible for 39% of all carbon emissions in the world [1], with the upfront/embodied emissions (associated with materials and construction processes) accounting for 11% [2]. To this end, one crucial strategy for reducing embodied carbon footprints of the building sector is to promote/ensure material utilisation, waste reduction, reuse of building components/products, and recycling materials as much as possible [3-6]. In this background, steel MBS, underpinned by modern methods of construction (MMC), design for manufacture and assembly (DfMA) methodology, and design for deconstruction (DfD) considerations, have become an increasingly viable proposition owing to their advantages such as faster construction speed, reduced waste generation, demountability and reusability, safer manufacturing, and better quality control [7-12]. In volumetric modular construction as shown in Fig. 1 (a), factory-made building modules are prefabricated off-site and subsequently transported to construction sites for final assembly to form a complete building through inter-module connections, as demonstrated in Fig. 1(b). In order to maximise the above benefits, MBS are best suited for tall building structures with repetitive units such as apartments, offices, student accommodations, hotels, and healthcare facilities [10,13]. Nevertheless, their application to date concerns mostly low- and mid-rise, with the number of tall modular buildings constituting less than 1% [14], due to several plausible causes. First, there is a lack of pertinent design provisions on the legislation level such that the current modular design practices are mostly based on codes/guidelines for conventional building structures [9]. Secondly, the structural behaviours of tall modular buildings in terms of integrity, stability, and serviceability needs to be better understood, especially under the dynamic action of strong wind and earthquakes [10]. Thirdly, despite a plethora of inter-

module joints [cf., 15-20] existing in the literature, the current state-of-the-art joining techniques are only able to achieve partial satisfaction in fulfilling manufacturing, constructional, and structural requirements [18]. Finally, difficulties can also arise due to transportation restrictions on module sizes/weights and the limited lifting capacities of tower cranes [21].

Another important topic of MBS, which has received scant attention in the literature and thus warrants further research, is the structural efficiency and material consumption of MBS compared to conventional building (structural) systems within a performance-based design context. Indeed, modular buildings can be material-intensive/demanding due to double beams and double columns coming from adjacently placed modules, as well as due to relatively short spans of modular units as opposed to long spans achieved in conventional MRFs. The latter is also attributed to the restrictions imposed on module sizes/weights for transportation and erection. In this regard, structural sizing optimisation (SO) is arguably the most commonly applied technique for automating code-compliant, material-efficient building designs whose structural layout requires minor or no shape/topology improvements. Typically, SO aims to minimise self-weight of the structure while ensuring satisfaction of certain prescribed performance criteria/constraints. For tall building applications, these constraints are usually given as lower limits on the natural frequencies or critical buckling loads or as upper limits on permissible nodal displacements/accelerations or member stresses under external loads [22-25]. Incidentally, several technical challenges of modular systems and construction listed previously can be collectively addressed by incorporating SO into the design process, enabling safer, stiffer, and economical tall modular buildings that are also resilient to wind and seismic effects. In addition to employing advanced design tools, innovative lightweight energy-dissipating devices, such as inerter-based dynamic vibration absorbers for mitigating wind- and earthquake-induced vibrations in buildings [26-29] and novel slider devises for seismic protection of modular buildings [30-33], may also be deployed to help modular buildings achieve performance targets in a more cost-effective manner. Furthermore, on the module level, SO can lead to lightweight modular units with reduced material wastes and construction costs that are also easier to transport and handle on-site, thereby further reducing operational and embodied carbon emissions due to manufacturing, transportation, and installation/construction.

In pursuit of efficient material use, Gatheeshgar et al. [21] recently applied the particle swarm optimisation technique to enhance the flexural resistance of cold-form steel beams with web perforations for modular

building applications. A conceptual MBS design comprising optimal cold-form steel members was developed to demonstrate the potential of structural optimisation in creating sustainable and material-efficient MBS design. Moreover, Gatheeshgar et al. [34] introduced the concept of employing optimised hollow flange beams to enhance the structural performance of MBS. Nevertheless, these two studies focused only on employing optimisation techniques at the local/member level; to the authors' best knowledge, there remains a scarcity of research on applying structural optimisation at the global/structure level to enhance MBS's overall structural performance and material efficiency.

Consequently, this paper attempts to addresses the above research gap through an innovative minimum-weight design investigation involving a three-storey MBS and a comparative MRF under a *generalised* stiffness constraint stated in the resonant/natural frequency. The overarching aims of the study are twofold: first, introducing a novel optimisation framework for pursuing continuous- and discrete-valued minimum-weight design of MBS subjected to natural frequency constraints; and second, comparing the self-weights of two optimally designed structural systems (i.e., MBS versus MRF) required to achieve a prescribed level of overall lateral stiffness, hence gauging the structural/material efficiency of MBS compared to conventional MRFs. The continuous SO of both structures is achieved by a novel OC-based sizing algorithm; the latter is proven to be computationally more efficient (in terms of convergence speed) than the conventional OC methods based on the uniform strain energy density criterion (cf., [23, 35-38]), which can become erratic for eigenvalue-constrained problems [39]. The sizing process is expedited by a high-quality estimating technique for efficient gradient/sensitivity analysis of design constraints, such that the proposed sizing algorithm can handle large design problems at relatively low computational cost. In support of practicality, the discrete minimum-weight design of MBS and MRF is achieved by employing a novel mapping technique to convert the continuous optimum to the nearest discrete solution using selected standard steel sections. Attention is focused on the convergence behaviour and numerical robustness of the sizing algorithm proposed, as well as on quantifying the self-weight reduction of the MBS achieved by the minimum-weight design method in lieu of the MRF comparative structure.

The remainder of the paper is organised as follows. In Section 2, the SO problem of frame structures (i.e., structures comprising frame elements) is defined for a single frequency constraint imposed on an arbitrary vibration mode. The method of Lagrangian multipliers is applied to formulate a frequency-related OC that

defines the optimality in a set of necessary conditions involving sensitivities of the constraint to the cross-sectional areas of modular members. A sizing algorithm is next established based on the derived OC for updating the member sizes and the Lagrangian multiplier in the continuous design space, followed by the presentation of a discrete minimum-weight design method assuming standard open and close steel sections. The numerical stability/robustness of the sizing algorithm is examined in Section 3 for a three-storey modular testbed model with two different sets of initial cross-sections under the same frequency constraint on the fundamental vibration mode. Next, in Section 4, the minimum-weight design method is applied to the three-storey MBS and the MRF benchmark structure for two frequency constraints imposed on the fundamental and second vibration modes separately. Comprehensive numerical results are furnished and discussed, shedding light on the material efficiency of MBS compared to conventional MRF systems. Finally, Section 6 summarises the main conclusions and recommendations for further research work. The accuracy, efficacy, and computational efficiency of the proposed sizing design method in Section 2 are demonstrated in Appendix A using a planar portal frame under a single frequency constraint. The OC formulation and sizing algorithm in Section 2, which are limited to a single frequency constraint, are generalised in the Appendix B for tackling multiple frequency constraints.

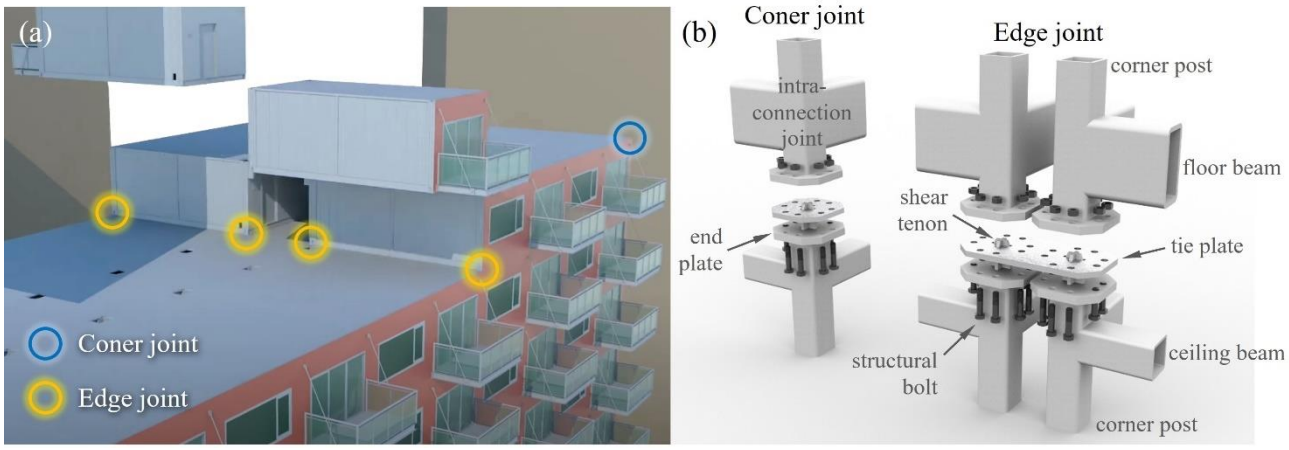

Fig. 1 (a) a modular building with corner and edge inter-connection joints only (VectorBloc corp., (2016). *VectorBloc Standardized Modular Construction System*); and (b) assembly view of newly developed corner and edge inter-module joints for minimum-weight design investigation in this study.

2. FORMULATION OF OPTIMALITY CRITERION AND SIZING ALGORITHM

In this paper, the natural frequency of a frame structure is adopted as a metric for quantifying its overall lateral stiffness associated with a particular vibration mode. Then, within an optimal (i.e., minimum-weight) design setting, the structure with lower self-weight is considered to be more efficient than the one that requires more structural material to reach the same resonant frequency. More precisely, efficiency here is quantified as the ratio of the natural frequency (of a particular vibration mode) to the amount of material (or self-mass) required by the structure to achieve that particular frequency. In this setting, an optimality criterion (OC)-based SO method is first presented herein for the minimum-weight design of frame structures of fixed layouts while satisfying a prespecified frequency constraint. Specifically, the OC methods rely on first characterising the optimal structure through some necessary conditions, which are believed to hold at the optimum, and then applying a resizing rule to gradually modify/resize the current design to satisfy these conditions, thereby indirectly optimising the structure. Compared to mathematical programming techniques and evolutionary computing approaches, the main attractions of OC methods for large design problems are their computational efficiency [40], benign convergence behaviour [41], and simplicity for practical implementation [39].

In what follows, a frequency-based OC is first derived in section 2.1 based on the formulations in Venkayya [42]. The OC is stated in a set of mathematically defined, necessary conditions, expressed as a system of differential equations involving partial derivatives of the frequency constraint with respect to member sizes. Next, a numerically robust, iterative algorithm is developed in section 2.2 for updating the structure's member sizes as per the OC derived in section 2.1. Finally, a minimum-weight design method for frame structures, including but not limited to MBS, is presented in section 2.3.

2.1 Optimisation problem formulation and optimality criterion derivation

Herein, a sizing optimisation problem (OP), which aims to minimise the structural self-weight while satisfying a frequency constraint on an arbitrary vibration mode k, is first formulated. The considered OP for an elastic frame structure comprising m frame elements but only n active design variables (DVs) (note $n \leq m$) can be expressed as:

$$\mathbf{a}^{*} = \underset{\mathbf{a}^{\min} \le \mathbf{a} \le \mathbf{a}^{\max}}{\arg\min} \left\{ M(\mathbf{a}) = \sum_{i=1}^{n} \rho_i l_i a_i \right\} \quad \text{s.t. } f_k(\mathbf{a}) - f_{k,\text{target}} = 0 \tag{1}$$

where $M(\mathbf{a})$: $\mathbb{R}^n \rightarrow \mathbb{R}$ is the objective function, measuring the total mass of structural material to be minimised. Furthermore, ρ_i, l_i, and a_i (i=1,…,n) represent the material density, fixed member length, and cross-sectional area of frame i, respectively. In the above formulation, the n cross-sectional areas, a_i (i = 1, …, n), are the *continuous-valued* DVs of the OP grouped in the vector $\mathbf{a} \in \mathbb{R}^{1\times n}$ and bounded by the side constraint $\mathbf{a}^{\min} \le \mathbf{a} \le \mathbf{a}^{\max}$. Specifically, the lower bound $\mathbf{a}^{\min}$ of the side constraint needs to ensure that the structure meets minimum displacement-based and strength-based (including buckling resistance) requirements under all load combinations in line with pertinent design codes, whereas the upper bound $\mathbf{a}^{\max}$ may be established by other considerations such as architectural and/or functional requirements. In addition, there are also m-n inactive members whose sectional properties remain constant during the SO process. Additional equal size constraints, which enforce sizes of certain structural members remaining the same during the sizing iteration, may be additionally imposed on active DVs in support of design practicality (see next section). The behavioural constraint in Eq. (1) requires that the structure's k-th natural frequency, $f_k(\mathbf{a})$: $\mathbb{R}^n \rightarrow \mathbb{R}$, is equal to a prespecified target value, $f_{k,\text{target}}$. The frequency for mode k in Eq. (1) can be evaluated by the expression:

$$f_k(\mathbf{a}) = \frac{\sqrt{\boldsymbol{\varphi}_k^T(\mathbf{a})\mathbf{K}(\mathbf{a})\boldsymbol{\varphi}_k(\mathbf{a})}}{2\pi}, \tag{2}$$

in which $\mathbf{K}(\mathbf{a})$ is the structural stiffness matrix and $\boldsymbol{\varphi}_k(\mathbf{a})$ is the k-th mode shape vector normalised such that $\boldsymbol{\varphi}_k^T\mathbf{M}\boldsymbol{\varphi}_k$=1 where $\mathbf{M}$ is the structure's mass matrix.

To facilitate a solution to Eq. (1), the method of Lagrange Multipliers is employed to convert the constrained OP in Eq. (1) into an unconstrained form. Specifically, the Lagrangian, $L(\mathbf{a},\lambda)$: $\mathbb{R}^n \times \mathbb{R} \rightarrow \mathbb{R}$, that adjoins the nonlinear behavioural constraint to the linear objective function is formed as:

$$L(\mathbf{a},\lambda) = M(\mathbf{a}) - \lambda\left[\, f_k(\mathbf{a}) - f_{k,\text{target}} \,\right], \tag{3}$$

where λ is the multiplier. Assuming $f_k(\mathbf{a})$ is differentiable on the feasible solution set of the OP, the stationary condition of the Lagrangian in Eq. (3) with respect to active DVs, i.e., $\nabla_{\mathbf{a}} L(\mathbf{a}, \lambda)=0$, yields the following equation:

$$\frac{\lambda}{\rho_i l_i}\frac{\partial f_k(\mathbf{a})}{\partial a_i} = 1 \ (i=1,....,n), \tag{4}$$

which defines the OC for the sizing OP in Eq. (1) in terms of n differential equations. Further, the stationary condition of the Lagrangian with respect to the multiplier, $\nabla_{\lambda} L(\mathbf{a}, \lambda)=0$, yields the behavioural constraint in Eq. (1), i.e.,

$$f_k(\mathbf{a}) - f_{k,\text{target}} = 0, \tag{5}$$

which is independent of the multiplier. Therefore, Eqs. (4) and (5) define a system of n+1 coupled equations for n+1 unknowns. These are the n cross-sectional areas (i.e., the active DVs) plus the multiplier λ.

As a remark, the OP in Eq. (1) is strictly convex [43] such that there exists one stationary point in the feasible solution set at most for Eq. (4) to hold. Moreover, if such a stationary point exists, it must be the global minimum $\mathbf{a}^*$ to the OP, as for strictly convex OPs a local optimum is also a global optimum [44]. Assured by this fact, the OC in Eq. (4) can be used to devise a finite element-based numerical procedure to refine/update the DVs iteratively towards the global optimum $\mathbf{a}^*$ at which the frequency constraint is satisfied with the minimum self-weight possible.

2.2 Sizing algorithm for frequency-constrained optimisation problems

Herein, a novel sizing algorithm is presented for iteratively modifying the DVs in accordance with the OC defined in Eq. (4) towards the global optimum $\mathbf{a}^*$. In OC-based sizing methods, the update formulas (for modifying DVs) utilise the DV vector $\mathbf{a}$ of dimension n and can take various forms, e.g., exponential, linearised,

reciprocal, or melange (cf., [45,46]). The vector **a** is then calculated from the stationary/optimality conditions by scaling, component by component, with respect to the gradient of the Lagrangian function [39]. In the current study, a *linearised* recursive relation for updating the DVs at iteration p attains the form:

$$a_i^{(p+1)} = a_i^{(p)} \left\{ 1 + \frac{1}{\eta} \left[\frac{\lambda^{(p)}}{\rho_i l_i} \left(\frac{\partial f_k(\mathbf{a})}{\partial a_i} \right)^{(p)} - 1 \right] \right\}, \tag{6}$$

where the term in the curly brackets is a scaling factor at iteration p for DV i and is devised directly from Eq. (4). Moreover, in the last equation, the relaxation parameter η controls the convergence rate of the sizing process: as η becomes smaller, the value of $a_j^{(p)}$ is modified to a larger extent, and vice versa. Suggestion regarding how to select η value is given in the next section for an illustrative example. The k-th natural frequency at iteration p, $f_k^{(p)}$, can be numerically evaluated using Eq. (2) by setting $\mathbf{K} = \mathbf{K}^{(p)}$ and $\boldsymbol{\varphi}_k = \boldsymbol{\varphi}_k^{(p)}$, where $\mathbf{K}^{(p)}$ and $\boldsymbol{\varphi}_k^{(p)}$ denote the structure stiffness matrix and k-th mode shape at iteration p, respectively.

Before utilising Eq. (6) to update the current design $\mathbf{a}^{(p)}$, it is necessary for the unknown multiplier at the current iteration, i.e., $\lambda^{(p)}$, to be known. To this aim, the change in the k-th frequency between two consecutive iterations, p and p+1, is firstly expressed by the approximation to a first-order Taylor series expansion about the DVs as:

$$f_k^{(p+1)} - f_k^{(p)} = \sum_{i=1}^{n} \left(\frac{\partial f_k}{\partial a_i} \right)^{(p)} (a_i^{(p+1)} - a_i^{(p)}) \tag{7}$$

Upon substituting Eq. (6) into Eq. (7) and assuming the behavioural constraint in Eq. (5) is satisfied after p iterations (such that $f_k^{(p+1)} = f_{k,\text{target}}$), the following relation for the multiplier at iteration p is established after some algebraic manipulation:

$$\lambda^{(p)} = \frac{\sum_{i=1}^{n} \left(\partial f_k / \partial a_i\right)^{(p)} a_i^{(p)} + \eta\left(f_{k,\text{target}} - f_k^{(p)}\right)}{\sum_{i=1}^{n} \left[\left(\partial f_k / \partial a_i\right)^{(p)}\right]^2 a_i^{(p)} / (\rho_i l_i)} \tag{8}$$

At this junction, suppose a stationary point exists in the feasible solution set, the iterative application of Eq. (6) for $a_i^{(p+1)}$ and Eq. (8) for $\lambda^{(p)}$ until convergence of the k-th frequency, $f_k(\mathbf{a})$, self-weight, $M(\mathbf{a})$, and the multiplier, λ, will provide the global optimal solution $\mathbf{a}^*$ to the OP in Eq. (1) subjected to the frequency constraint in Eq. (5).

Note in using Eqs. (6) and (8) for updating the DVs and the multiplier, respectively, partial derivatives of the constraint function with respect to active DVs, i.e., $\partial f_k^{(p)}/\partial a_i$ (i=1,…,n), are required. In this regard, an efficient numerical procedure is needed for rapid gradient calculation of the natural frequency. To this aim, the frequency for mode k at iteration p, $f_k^{(p)}$, is first expressed in terms of structure stiffness matrix $\mathbf{K}(\mathbf{a})^{(p)}$ and corresponding mode shape vector $\boldsymbol{\varphi}_k(\mathbf{a})^{(p)}$ using Eq. (2). Then, derivatives of $f_k^{(p)}$ can be approximated using following formula according to Wittrick [47]:

$$\frac{\partial f_k^{(p)}}{\partial a_i} = \frac{1}{4\pi\sqrt{\boldsymbol{\varphi}_k^T \mathbf{K}(\mathbf{a}) \boldsymbol{\varphi}_k}} \left(\boldsymbol{\varphi}_k^T \frac{\partial \mathbf{K}}{\partial a_i} \boldsymbol{\varphi}_k\right)^{(p)} \quad (i = 1, ..., n), \tag{9}$$

Finally, the derivatives of structure stiffness matrix $\mathbf{K}^{(p)}$ at iteration p in Eq. (9) can be evaluated conveniently using the equation below:

$$\left(\frac{\partial \mathbf{K}}{\partial a_i}\right)^{(p)} = \frac{\mathbf{K}^{(p)} - \mathbf{K}_i^{(p-1)}}{a_i^{(p)} - a_i^{(p-1)}}, \tag{10}$$

where $\mathbf{K}_i^{(p\text{-}1)}$ is a mixed structure stiffness matrix in which the element stiffness matrix for member i is from the previous iterative step p-1 while the remaining element stiffness matrices are from the current step p. As a remark, at the initial step p=1, the element stiffness matrix for member i from the "previous" iterative step, p=0,

is set to a zero matrix.

At this point, it needs to emphasise that the above sizing algorithm is continuous-valued, whereas the DVs in realistic optimisation/design problems can only attain discrete values. In this context, a minimum-weight design method, featured with a mapping/rounding technique, is presented in the upcoming section to support the discrete optimal design of MBS subjected to a single frequency constraint. This technique allows one-to-one mapping of continuous-valued, optimal sectional properties onto a list of standard steel sections.

2.3 Discrete minimum-weight design method for modular building systems

With the SO algorithm in the last section, the discrete minimum-weight design of MBS under a frequency constraint can be achieved in an automated manner by going through a three-step procedure as shown in Fig. 2 and detailed below:

(I) Initially, the target frequency for mode k, $f_{k,\text{target}}$, is first specified. Frame members of the structure and corresponding DVs are then separated into active and inactive sets. As aforementioned, only active DVs are modified in the SO process, whereas inactive DVs remain invariant. Side constraints on the active DVs, i.e., $\mathbf{a}_{\min} \leq \mathbf{a} \leq \mathbf{a}_{\max}$, are established based on strength-based and displacement-based requirements according to pertinent design codes.

(II) Next, the SO algorithm in section 2.2 is applied to update the active DVs of the structure until concurrent convergence of the k-th frequency, f_k , self-weight, $M(\mathbf{a})$, and Lagrangian multiplier, λ. During the sizing iteration, the DVs are *unbounded* by the side constraint in step (I), i.e., $\mathbf{a}_{\min} \leq \mathbf{a} \leq \mathbf{a}_{\max}$, so that the sizing algorithm can drive the current design towards the global optimum that satisfies the OC in Eq. (4). Only upon convergence, the continuous-valued sectional properties are compared with the respective side constraints. If any side constraint is violated by the current optimal solution $\mathbf{a}^{*(s)}$, the active and inactive DV sets initialised in step (I) are modified and updated. Specifically, the DVs falling outside their respective constraints are changed from active to inactive and are forced to their bound values. The SO process is then re-executed with the same target frequency by setting $s=s+1$. This process is executed repeatedly until no side constraint is violated by any DV, at which point the sizing process is considered to be converged and optimal sectional properties of all member groups are retrieved. For three dimensional

Euler-Bernoulli beam elements, the sectional properties should at least include $\mathbf{a}\in\mathbb{R}^{1\times n}$, $\mathbf{I}_{yy}\in\mathbb{R}^{1\times n}$, $\mathbf{I}_{zz}\in\mathbb{R}^{1\times n}$, $\mathbf{J}_t\in\mathbb{R}^{1\times n}$, where $\mathbf{I}_{yy}$ and $\mathbf{I}_{zz}$ are two vectors collecting second moments of inertia about major and minor bending axes of active frame members, separately, and the vector $\mathbf{J}_t$ collects the torsional constants.

(III) Finally, the continuous-valued optimal sectional properties, obtained in step (II), are mapped onto a list of standard steel sections of choice. For frame structures, this one-to-one mapping can be conveniently done by selecting a steel section in that list whose major second moment of inertia, I_{yy}, just exceeds the corresponding optimal value, I_{yy}^*, but with the minimum cross-sectional area possible to reduce the structural self-weight. This mapping strategy is proven to be quite effective for frame structures that resist lateral loads by bending, as will be seen in section 4.

As final remarks, it is worth to emphasise that a design that satisfies the OC in Eq. (4) and the theoretical optimum to the OP in Eq. (1) are synonymous *only* in the case of a single load condition and no side constraints on member sizes [38]. To this effect, the SO iteration in step (II) is unbounded initially; it is not until the convergence of the sizing iteration that the side constraints are verified, with active and inactive DV sets updated for the next round of sizing iteration. The correctness of the continuous-valued sizing algorithm in Section 2.2 and efficacy of the mapping strategy proposed herein (for discrete design) are demonstrated in Appendix A using a planar MRF structure under a single frequency constraint. Further, although the OC formulation in section 2.1 and the sizing algorithm in section 2.2 are derived for frequency-constrained problems, they are readily amenable to tackling displacement-, stress-, and buckling-constrained sizing problems of frame structures as well. This adaptation can be conveniently done by replacing the frequency constraint in Eq. (1) with another type of performance constraint, e.g., a lower limit on critical buckling load, or upper limits on either nodal displacements or member stresses. However, in the latter two cases, there are usually more than one performance constraints to consider in the design, which need to enter the OP formulation with a unique Lagrangian multiplier as a "weighting factor". Then, it is not a trivial task at all to determine whether a particular displacement/stress constraint is active or passive and, if active, the constraint's contribution to the overall performance requirement [48]. Further difficulties can arise from the need to initialise the values of Lagrangian multipliers at the start of sizing iteration, which can heavily affect the convergence behaviour of the OC methods [49]. In this context, the minimum-weight design in this work only considers a single frequency constraint.

Nevertheless, the OC formulation and sizing algorithm presented in this section are extended to multiple frequency constraints in the Appendix B for theoretical completeness.

In the upcoming section, the SO algorithm in section 2.2 is applied to an illustrative example subjected to a frequency constraint on its fundamental vibration mode to demonstrate the algorithmic robustness/numerical stability for MBS.

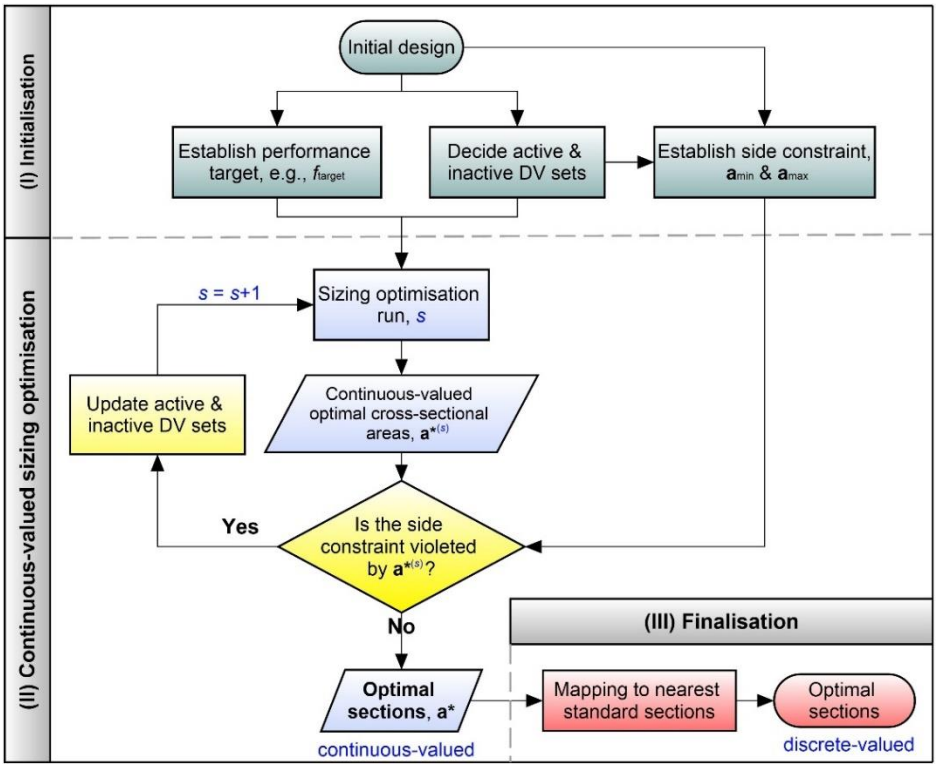

Fig. 2 Flowchart of discrete minimum-weight design method for frequency-constrained optimisation problems of frame structures in general.

3. ILLUSTRATIVE APPLICATION

In this section, the SO numerical routine in Section 2.2, based on an in-house finite element (FE) code for modal analysis of 3-dimensional frame structures, is implemented in MATLAB® and applied to a modular building's FE model for self-weight minimisation under a frequency constraint on its fundamental mode. In section 3.1, attention is first turned to the effects of inter-module joints' end releases on dynamic attributes of the modular building model. Next, a method for expressing sectional properties of standard open and close steel sections in

terms of cross-sectional areas in closed form through regression analysis is presented in section 3.2. This expression is essential in the sizing algorithm for deriving element stiffness matrices of frame elements using their cross-sectional areas only. In section 3.3, the sizing algorithm's convergence behaviour and numerical stability/robustness are demonstrated and discussed in detail, using the modular building model presented in section 3.1.

3.1 Effects of inter-connection joint end release on dynamic attributes of modular building systems

As shown in Fig. 3, the testbed model adopted for illustration of the sizing algorithm is a three-storey modular building consisting of nine modular units; the latter are connected through bolted corner and edge inter-module joints with shear tenons and tie plates, as shown in Fig. 1(b). A single modular unit is 6m long, 3m wide, and 3m high, while other dimensions of the building model are fully given in Fig. 3. Corner posts of the modules are made of square hollow sections SHS120/6.3, ceiling and floor beams are made of rectangular hollow sections RHS150×100/6.3 and RHS180×100/6.3, respectively. The second moments of inertia (about the major bending axis) of these sections follow closely a mid-rise modular building reported in the literature (see [50]). As shown in Fig. 1(b), modular beams are welded directly to the flanges of corner posts, such that the intra-connection joints where the ceiling/floor beams meet the corner post are taken as perfectly rigid. Further, the corner and edge joints are modelled using Timoshenko beam elements to take into account the shear deformation effects of deep/short beams, as shown in the zoomed-in windows in Fig. 3. For the sake of brevity, the beam elements used to model the vertical interconnection between upper and lower modules are referred to as vertical joint beams hereafter, whereas the beams representing the tie plate (see Fig. 1(b)) are referred to as horizontal joint beams. At this point, it should be noted that modelling bolted inter-module joints using beam elements with appropriate end releases is common practice in the scientific literature for simplifying and facilitating global analysis of MBS (cf., [51-55]). In this type of simplified joint model, the intra-connection joints are generally taken as rigid, whilst a pinned joint is used to capture the independent rotation between the upper and lower corner posts [56]. Accuracy of this modelling technique is verified with experimental data by Annan et al. [57]. For the testbed model, two end-release scenarios are considered for the inter-connection joints in parallel. In the first scenario as depicted by Fig. 3(a), the corner and edge joints are fully fixed at both ends so that bending moment can transfer between adjacent corners of modular units. In the second scenario as depicted in Fig. 3(b),

a hinge is assigned at the middle point of the vertical joint beams to release biaxial bending at that node. Moreover, for edge joints, the horizontal joint beams are released for bending moment about the horizontal bending axis. In this setting, the first scenario serves as the most conservative simplification of the bolted joints in Fig. 1(b), whereas the second is the least conservative approximation.

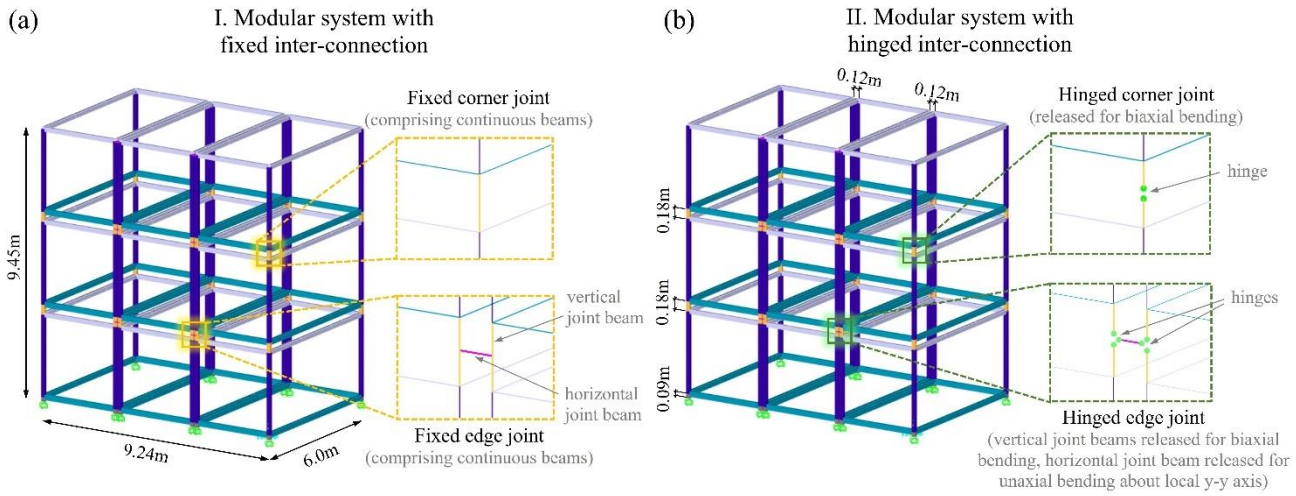

Fig. 3 A three-storey modular system with (a) fixed and (b) hinged inter-connection joints.

Firstly, standard modal/eigenvalue analysis is performed to the modular system in Fig. 3 with two different joint rigidities in SAP2000® software package by assuming identical mass source, i.e., structural self-weight + superimposed load + 0.3 live load. Specifically, the superimposed load acting on the ceiling and four walls of the modules are taken as 0.5KPa, while the imposed load is increased to 2.0KPa for the floor. A live load of 2.0 KPa is applied on the floor of all modules. The imposed mass due to superimposed and live loads is lumped at the corner joints only, whereas the self-mass (due to structural members) is lumped at both ends of meshed frame elements. The first six natural frequencies of the modular system in Fig. 3 and corresponding modal assurance criterion (MAC) values between the two end-release scenarios are calculated by SAP2000 and summarised in Table 1. Herein, the MAC value for mode *j* measures the mode shape similarity between the two inter-connection rigidities and is defined as (see [58]):

$$\mathrm{MAC}_j = \left(\frac{\boldsymbol{\varphi}_{j,\mathrm{fixed}}^T \boldsymbol{\varphi}_{j,\mathrm{hinged}}}{\left\|\boldsymbol{\varphi}_{j,\mathrm{fixed}}\right\| \left\|\boldsymbol{\varphi}_{j,\mathrm{hinged}}\right\|} \right)^2, \tag{11}$$

where $\boldsymbol{\varphi}_{j,\mathrm{fixed}}$ and $\boldsymbol{\varphi}_{j,\mathrm{hinged}}$ are the j-th mode shape vectors of the testbed model with fixed and hinged inter-connection joints, respectively, the superscript "T" denotes vector transposition, and $\|\boldsymbol{\varphi}\|$ is the length of vector $\boldsymbol{\varphi}$. Clearly, MAC_j value equal to unity means that the two mode shape vectors are identical, whereas MAC_j value equal to zero indicates zero degree of consistency/similarity between the two mode shapes.

It is seen in Table 1 that the testbed model with hinged inter-connection joints has always slightly smaller natural frequencies. Nevertheless, for the first four vibration modes, the percentage errors in natural frequency between the two models are smaller than 3% (see values in paratheses) with the MAC values always above 0.998. This observation implies that the end release of inter-module joints in Fig. 3(a) have negligible impacts on modal attributes up to mode 4. However, in vibration modes 5 and 6, the difference in frequency starts to increase with the MAC values dropping to zero, meaning that the two models have fundamentally different mode shapes. This observation is consistent with the findings in Lacey et al. [59], which shows that the overall lateral stiffness of modular buildings is mainly affected by shear stiffness of vertical inter-module connections but not by their rotational stiffness. In this context, given that the SO in this work always targets at either the fundamental or second vibration mode, it is therefore deemed conservative and appropriate to assume hinged inter-connection joints for the rest of numerical investigation.

Table 1. Comparison of modal attributes of the modular system with fixed inter-connection joints as in Fig. 3 (a) and hinged inter-connection joints as in Fig. 3 (b), values computed by SAP2000 and MATLAB FEA tool.

Modular system	Program	Natural frequency [Hz] and modal assurance criterion [1]					
		1st mode	2nd mode	3rd mode	4th mode	5th mode	6th mode
I. with fixed connection	SAP2000	0.965	1.049	1.216	2.597	2.731	2.839
	MATLAB	0.964	1.042	1.193	2.455	2.808	2.917
II. with hinged	SAP2000	0.937	1.023	1.186	2.574	2.595	2.595

connection		(-2.90%)	(-2.48%)	(-2.47%)	(-0.89%)	(-4.89%)	(-8.59%)
	MATLAB	0.937	1.023	1.202	2.447	2.562	2.704
MAC between I & II	SAP2000	0.9990	0.9997	0.9994	0.9988	0.0000	0.0000
MAC between MATLAB & SAP2000 for scenario I		1.0000	0.9999	0.9997	0.9976	0.9969	0.9982
MAC between MATLAB & SAP2000 for scenario II		1.0000	1.0000	0.9998	0.9981	0.9995	0.9983

Finally, to examine the accuracy of the FE code developed in MATLAB® for later sizing optimisation, two additional modal analyses are performed for the same modular system with two different inter-connection joint rigidities in Figs. 3 (a) and (b), separately. For both end-release scenarios, the first six natural frequencies and MAC values between the mode shapes predicted by SAP2000 and MATLAB code are added in Table 1. As seen, the difference between the two sets of resonant frequencies is negligibly small, with MAC values greater than 0.99 across all six vibration modes regardless of the inter-connection rigidity. Overall, the matching quality of modal properties in Table 1 proves the accuracy of the MATLAB FE code for modal analysis of 3-dimensional frame structures and its applicability for sizing optimisation workflow.

3.2 Expressing sectional properties in terms of cross-sectional area for standard open and close steel profiles

To use the iterative algorithm in section 2.2 for SO of the testbed model in Fig 3(b), it is necessary to express all sectional properties of each group of modular members as functions of the cross-sectional area/DV, a_i. For three-dimensional Timoshenko beams with twelve degrees of freedom, the sectional properties for element i should include a_i, $A_{yy,i}$, $A_{zz,i}$, $I_{yy,i}$, $I_{zz,i}$, and , $J_{t,i}$, where $A_{yy,i}$ and $A_{zz,i}$ are the shear areas in the frame element's local transverse and vertical directions, respectively, $I_{yy,i}$ and $I_{zz,i}$ are the second moments of inertia about major and minor bending axes, separately, and $J_{t,i}$ is the torsional constant of inertia. Previous studies by Chan [60] show that these sectional properties can be expressed as reciprocal functions of cross-sectional areas through

regression analysis. In addition, the widely used simple relationship $I_j = ca_j^r$ covers many practical cases where "*c*" and "*r*" are some constants depending on the type of steel sections [46]. Then, for RHS beams of the testbed model, above five sectional properties can be expressed as polynomial functions of cross-sectional areas through regression analysis as demonstrated in Fig. 4. The same strategy is also applicable to SHS and other types of standard close and open steel profiles. However, for the testbed model in Fig. 3(b), an additional constraint on the corner posts is that they need to maintain the same outer dimension, *b*, but can have different thicknesses, *t*, throughout the height. This consideration stems from the fact that changing the corner post size along the building height can, arguably, make the connection between adjacent modules more difficult [56]. Further, another constraint on the modular beams is that their widths must not exceed the outer dimension of the corner posts so that the beams can be fully welded to the columns. These two buildability constraints simply mean that the commercially available SHS and RHS profiles need to be pre-filtered for the SO workflow and the regression analysis is performed to those selected SHS and RHS profiles only. Finally, the formulas used to relate the sectional properties of RHS, SHS, and parallel flange I sections (IPE) to their cross-sectional areas are summarised in Table 2. Note in section 4, the MBS in Fig. 3(b) is compared against a conventional MRF with identical outer dimensions and imposed masses to gauge their structural/material efficiency in achieving a particular frequency. The MRF structure uses SHS for columns and IPE profiles for beams.

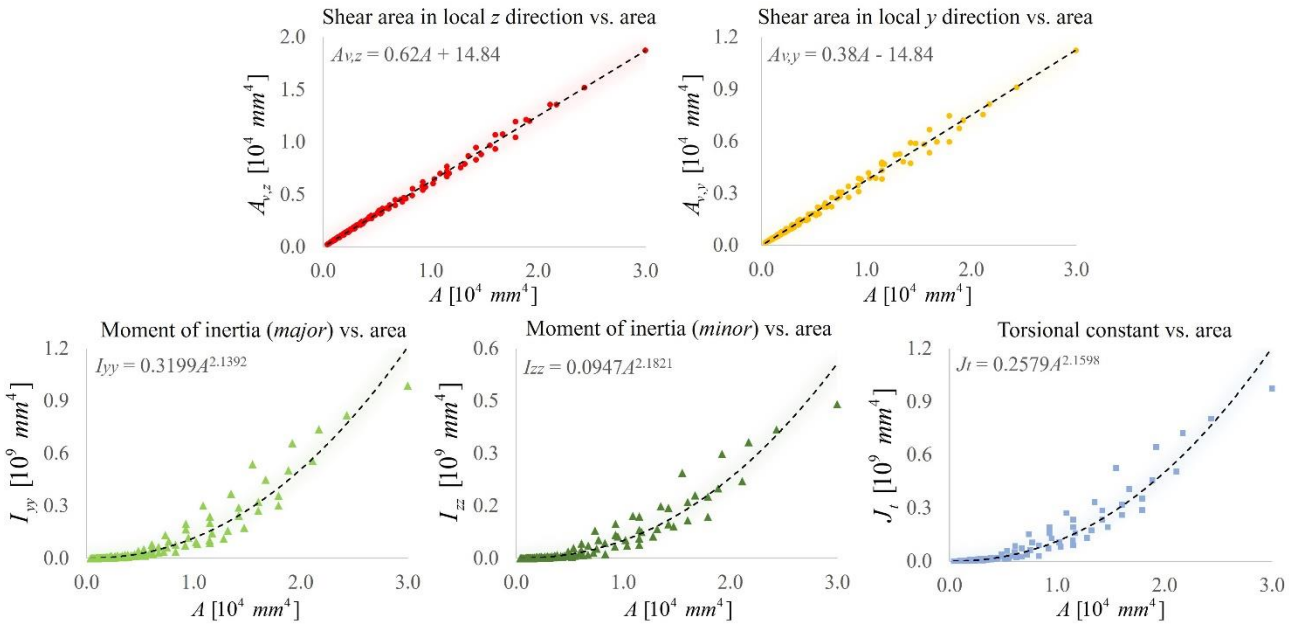

Fig. 4 Expressing sectional properties of rectangular hollow sections as polynomial functions of cross-

sectional area.

As a final remark, during the sizing process of the testbed model in Fig. 3(b), formulas in Table 2 are applied at the end of each DV update/iteration to evaluate shear areas and various moments of inertia of each group of members based on the updated cross-sectional areas $\mathbf{a}^{(p+1)}$ determined by Eq. (6). These sectional properties are then used to construct element stiffness matrices assuming Timoshenko beam model before assembly of structure stiffness matrix for next iteration p+1. Upon convergence, the continuous-valued optimal sectional properties are used to find the most economical standard sections (in terms of cross-sectional area) whose major second moment of inertia just exceeds the optimal value (see also step (III) in section 2.3). Note for the testbed model, the outer width of corner posts is fixed to its initial value of 120mm throughout the sizing process in the rest of numerical investigation.

Table 2. Formulas relating sectional properties of various standard steel sections and their cross-sectional areas.

Sectional properties	Steel sections		
	RHS	SHS	IPE
	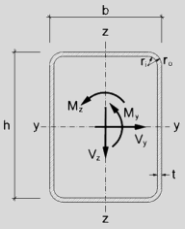	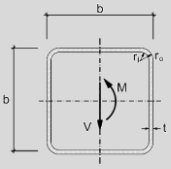	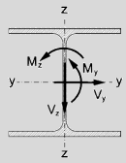
A_{vy} [mm^2]	A_{vy}=0.38A-14.84	A_v=0.50A-0.02	A_{vy}=0.54A+199.81
A_{vz} [mm^2]	A_{vz}=0.62A+14.84		A_{vz}=0.54A-169.66
I_{yy} [mm^4]	I_{yy}=0.3199$A^{2.1392}$	I=0.2238$A^{2.1405}$	I_{yy}=0.1799$A^{2.3209}$
I_{zz} [mm^4]	I_{zz}=0.0947$A^{2.1821}$		I_{zz}=0.1440$A^{2.0215}$
J_t [mm^4]	J_t=0.2579$A^{2.1598}$	J_t=0.3773$A^{2.1332}$	J_t=0.0348$A^{1.8218}$

3.3 Robustness/numerical stability of the sizing algorithm

Herein, attention is drawn to the convergence behaviour and numerical stability/robustness of the sizing

algorithm in section 2.2 for solving the frequency-constrained OPs of MBS formulated in section 2.1. The aim is to examine how different inputs (i.e., different initial designs) affect the algorithm execution and optimisation results. To this end, the testbed model in Fig. 3(b) is optimised for minimum self-weight by targeting at its initial fundamental frequency, i.e., $f_{1,\text{target}}$=0.937Hz. Cross-sections of corner posts, ceiling, and floor beams of this initial design are summarised in Table 3 under the name "design A", amounting to a self-mass of 10669.0 kg. In addition, a different design, termed "design B", with exactly the same setup but with different cross-sections reported in Table 3, is considered in parallel for SO by targeting at the same fundamental frequency of 0.937Hz. To better support the SO process, modular members are categorised into nine groups as listed in Table 3, by allowing the corner posts, ceiling beams, and floor beams to attain different cross-sections in different storeys. Moreover, the vertical joint beams are required to have the same cross-sections as the adjacent corner posts since they are a continuation of the corner posts from within the modules to the endplates, as shown in Fig. 1(b). In this setting, the only inactive members during the sizing process are the horizontal joint beams for modelling the tie plate in Fig. 1(b).

In Fig. 5, the variations in the normalised fundamental frequency (normalised by $f_{1,\text{target}}$=0.937Hz), normalised self-weight (normalised by 10669.0 kg), and the Lagrangian Multiplier (see Eq. (8)) throughout the SO processes of two designs in Table 3 are plotted in the subplots (a), (b), and (c), respectively. As seen in Fig. 5(a), the normalised frequencies of designs A and B both converge to 1.000 after 83 and 89 iterative steps, respectively, despite the fact that these two designs have very different initial fundamental frequencies. Similar observation can be made for normalised self-weights in Fig. 5(b) as well as for the Lagrangian Multiplier in Fig. 5(c). The self-weights are seen to decrease almost monotonically (except in the first a few steps) at a reducing rate and become practically flattened after step 70 for both designs. To shed light into the optimal solutions retrieved, the optimal cross-sectional areas, obtained from designs A and B, are summarised in Table 4, separately, with the average percentage error (APE) reported in the rightmost column. Here, the APE is defined as a ratio of the absolute difference between two values over the average of these two values. It can be seen that for all nine groups of modular members, the APE values between the two sets of optimal cross-sectional areas are smaller than 2.00% across the board, evidencing that the sizing algorithm is indeed numerically stable and is able to drive the current design towards the global optimum regardless of variation in the input.

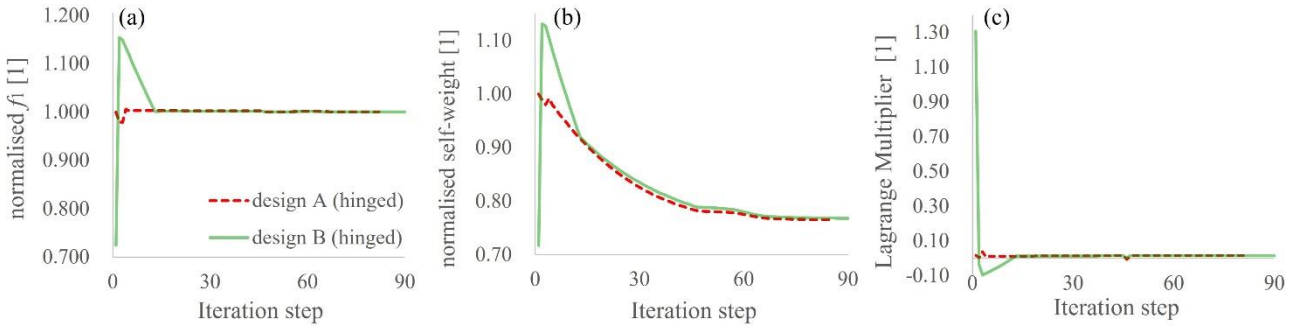

Fig. 5 Variations in (a) normalised fundamental frequency, (b) normalised self-weight, and (c) Lagrangian Multiplier throughout sizing optimisation process of the modular system in figure 3 with hinged inter-connection joints.

As a final note, for both optimisation runs behind Fig.5, the relaxation parameter, η (see Eq. (6)), is set to 50 between iteration steps 1 and 50, and is increased to 1000 from iteration step 51 onwards. In general, larger the η value is, smoother the convergence will be and more likely the algorithm will converge to the theoretical optimum. However, large η values can result in slow convergence so that some trial and error for selecting appropriate η values is required.

Table 3. Continuous-valued, optimal cross-sectional areas of two different designs of the modular system in figure 3 (b) with hinged inter-connection joints.

Member group		Initial cross-sectional area [mm^2]		Continuous-valued optimal cross-sectional area [mm^2]		
		Design A	Design B	Design A	Design B	APE
Corner posts	1st storey	2823 (SHS120/6.3)	3515 (SHS120/8.0)	4430.5	4545.1	0.64%
	2nd storey			2197.0	2246.6	0.56%
	3rd storey			1054.9	1108.9	1.25%
Ceiling beams	1st storey	2949 (RHS150×100/6.3)	1473 (RHS100×60/5.0)	3165.3	3094.6	0.56%
	2nd storey			2986.2	2916.4	0.59%
	3rd storey			1390.9	1301.4	1.66%

Floor beams	1st storey	3327 (RHS180×100/6.3)	1919 (RHS150×100/4.0)	1095.5	1157.3	1.37%
	2nd storey			3119.8	3132.2	0.10%
	3rd storey			1669.7	1734.5	0.95%

4. COMPARATIVE STUDY WITH TRADITIONAL MOMENT RESISTING FRAMES

In this section, the discrete minimum-weight design method in section 2.3 is applied to the modular building model in Fig. 6(a) (the same structure as in Fig. 3(b)) to showcase its usefulness and applicability for the optimal design of MBS under a generalised stiffness constraint stated in terms of resonant frequency. For comparative purpose, an ordinary three-storey MRF with identical outer dimensions and two different beam-to-column connection stiffnesses is considered in parallel as a benchmark structure to gauge the structural efficiency of MBS compared to conventional MRFs. In order to make the comparison fair and the investigation focuses solely on the MBS, both structural systems considered here are self-standing (i.e., without any additional lateral stability system) and without any bracing system.

4.1 Description of two comparative structural systems adopted for sizing optimisation investigation

For the modular system in Fig. 6(a), the vertical and horizontal joint beams are released for bending as in Fig. 3(b). The intra-connection joints are still assumed to be perfectly rigid, justified by the fact that the modular beams are welded directly to the corner posts as shown in Fig. 1(b). Steel sections used in the modular system are detailed in Table 3 under the name "design A", which uses one standard section for ceiling beams, floor beams, and corner posts throughout the building height, separately. As shown in Fig. 7, the modular system's first and second vibration modes are translational in the global y- and global x-directions, with the corresponding natural frequencies equal to 0.937Hz and 1.023Hz, respectively. In the next section, these two eigenvalues (of design A in Table 3) are adopted as the target frequencies for two independent minimum-weight designs of the modular system in Fig. 6(a) and the MRF benchmark structure in Fig. 6(b).

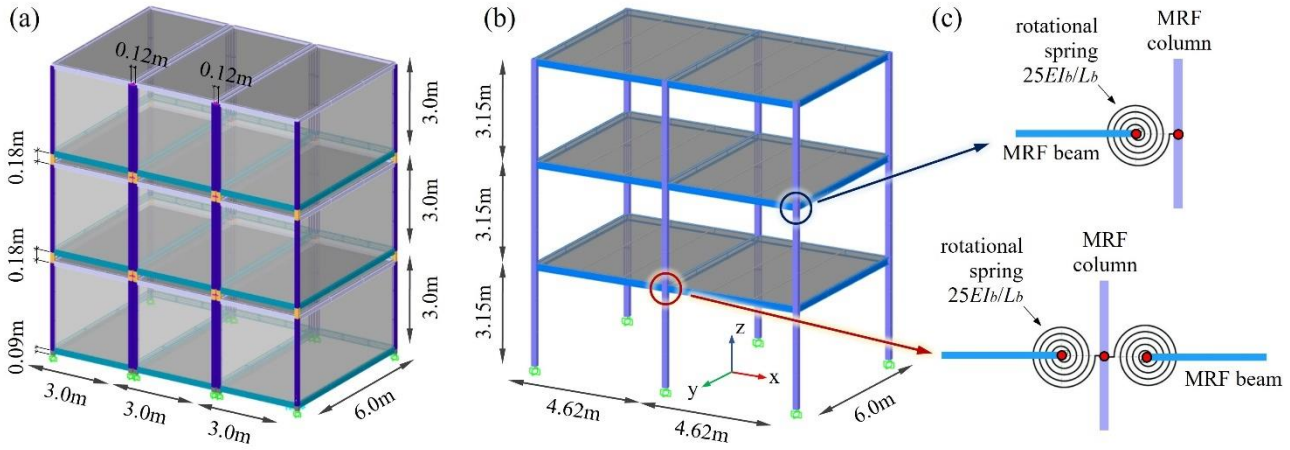

Fig. 6 Two comparative structures: (a) the modular system with hinged inter-connection joints, and (b) a moment resisting frame with two bays in global x-direction and one bay in global y-direction, and (c) the mechanical models used for modelling beam-column connections in the semi-rigid moment resisting frame.

For the MRF structure in Fig. 6(b), two beam-column connection stiffnesses are considered in parallel: perfectly rigid (as considered in the modular system) and semi-rigid as per Eurocode 3. In the latter case, a rotational spring with two degrees of freedom, as shown in Fig. 6(c), is added between the ends of ceiling/floor beams and the intermediate joint of corner posts. Its rotational stiffness is set to $25EI_b/L_b$, where E is the elastic modulus of structural steel, and I_b and L_b denote the (major) second moment of inertia and the length of the MRF beam, respectively. It needs to pointed out that this rotational stiffness value corresponds to the classification boundary between "rigid" and "semi-rigid" connections for unbraced frames in Eurocode 3 and thus by no means represent a rationally flexible connection. In support of lightweight design, standard IPE profiles are used for the MRF beams, while the MRF columns are still made of SHS with a constant/increased width of 160mm as opposed to 120mm for the modular system. For the MRF in Fig. 6(b), its first two vibration modes are also translational in the global y- and x-directions, respectively, irrespective of the beam-column connection stiffness. The same mass source used for modal analysis of the modular system in Fig. 6(a) is adopted for the MRF benchmark structure by applying an equivalent, uniformly distributed loading on the floor slabs in Fig. 6(b). In this setting, the two structural systems share the same imposed gravitational loads such that a fair and meaningful comparison can be made between the two structures.

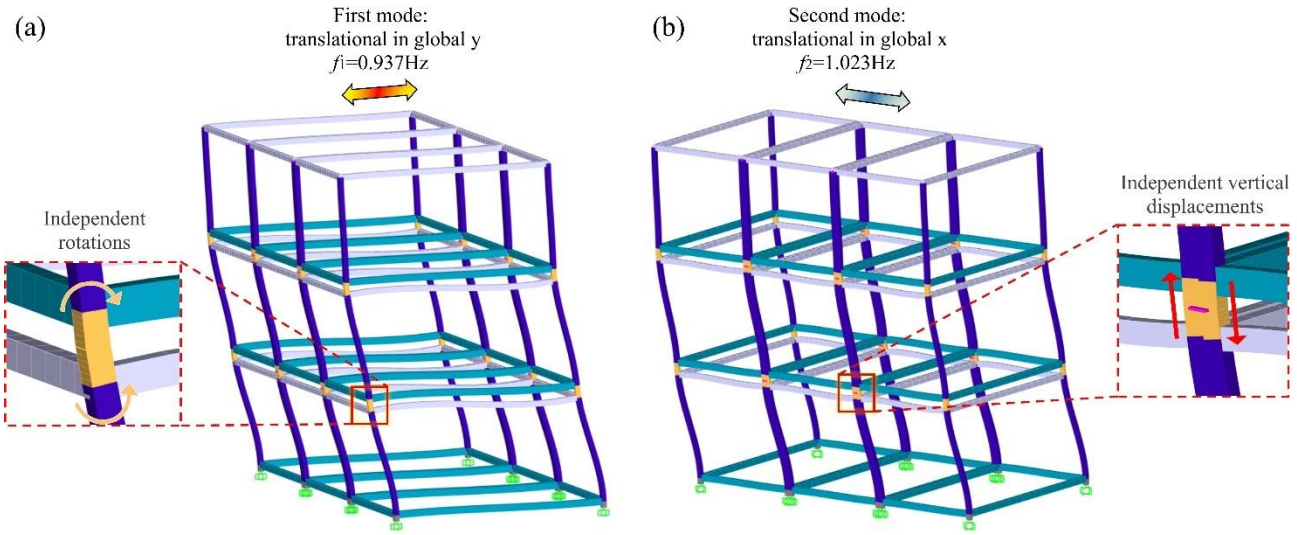

Fig. 7 (a) The first and (b) second vibration modes and corresponding deformation of inter-connection joints of the modular system in Figure 6(a).

4.2 Self-weight comparison with optimally designed MRFs

For the modular system and MRF structure in Figs. 6 (a) and (b), their minimum-weight design is firstly pursued for the fundamental vibration mode in the global y-direction (referred to as "first-mode optimisation" hereafter) and then for the second vibration mode in the global x-direction (referred to as "second-mode optimisation" hereafter), independently. The SO is facilitated by targeting the corresponding natural frequency of the initial modular design/design A in Table 3, i.e., $f_{1,target}$=0.937Hz for the first mode and $f_{2,target}$=1.023Hz for the second mode. In this setting, there are six SO runs and minimum-weight design processes in total, arising from the combination of three structures (i.e., one modular plus the MRF with two different connection stiffnesses) and two vibration modes for each structure considered. In all minimum-weight designs, the DVs (i.e., cross-sectional areas of frame members) are lower-bounded by standard sections that satisfy minimum displacement-based and strength-based (including buckling resistance) requirements under static, gravitational design load combinations according to Eurocode 3. To support the minimum-weight design, frame members of the modular system are categorised into nine groups as indicated in Table 4, while for the MRF structure, there are six member groups in total as listed in Table 5. Optimal standard sections obtained from the two minimum-weight designs are summarised in Table 4 for the modular system and in Table 5 for the MRF with semi-rigid connections only. Evidently, the more member groups are allowed in the optimisation, the better the optimisation outcome will be

and the smoother/easier it becomes for the continuous SO process to converge. However, from a practical standpoint, there is a trade-off between the structural material usage and buildability of a design, as it is impractical to allow each structural member to have a unique section.

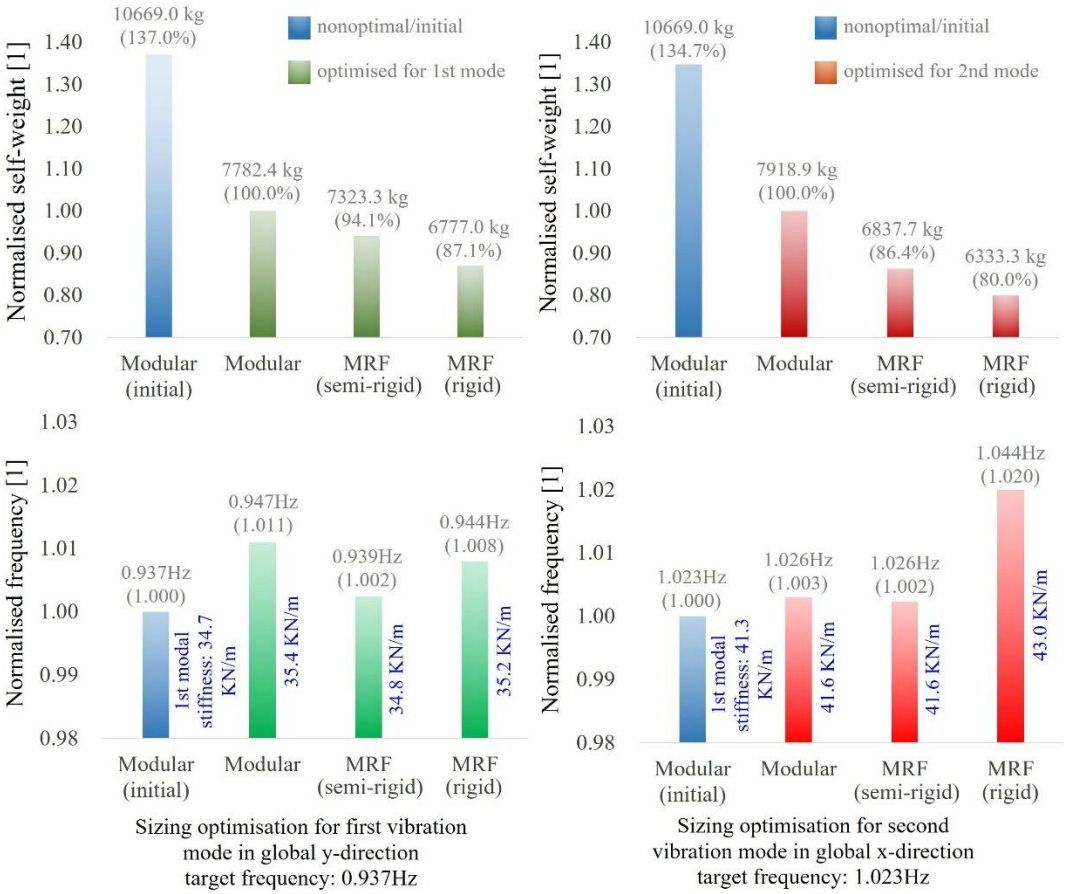

Fig. 8 normalised self-weights and natural frequencies of initial and optimal modular system and MRF structure with two different connection rigidities: (left) minimum-weight design is pursued in the global y-direction for the first mode, and (right) minimum-weight design is pursued in the global x-direction for the second mode.

To shed light on the potential gain on material saving, self-weights and corresponding natural frequencies of the initial and optimally designed modular systems are first bar-plotted in the left and right panels/columns of Fig. 8 for the first-mode and second-mode optimisations, respectively. For comparison, the same quantities of optimally designed MRF structure, with two different connection stiffnesses, are also furnished in Fig. 8 with the connection rigidity indicated in the parentheses. Specifically, the upper row of subplots in Fig. 8 is for

structural self-weights, normalised by the corresponding self-weight of optimally designed modular system such that the two bars for the optimised modular system always attain a height of 100.0%. Further, the lower row of subplots in Fig. 8 is for natural frequencies of the initial and optimally designed structures considered in the upper panel of Fig. 8; the values are normalised by the corresponding target frequencies used in the first-mode and second-mode optimisations, respectively. In order to render the results more direct to interpret, unnormalised modal stiffness values (in [KN/m]) of initial and optimised modular systems as well as of the optimised MRF with two different beam-column rigidities are augmented in the lower row of Fig. 8, right next to the vertical bars. Numerically, these modal stiffness values are equal to the corresponding circular frequencies squared, due to the normalisation of modal masses to 1.0. In this setting, the two blue bars in the lower panel of Fig. 8 for the initial modular system (i.e., design A in Table 3) both attain a height of 1.000, as its first two natural frequencies are used as the target frequencies for SO. As seen in the upper subplots, the optimal modular system reaches the target frequency of 0.937Hz (for the first vibration mode) and 1.023Hz (for the second vibration mode) with a self-weight of 7782.4 kg and 7918.9 kg, respectively. These self-weights correspond to a weight reduction of 27.1% and 25.8% compared to the initial modular design in Table 3, which has a self-weight of 10669.0 kg. Alternatively, one can also say that the initial modular design is 37.0% and 34.7% heavier than the optimal designs retrieved by the first-mode and second-mode optimisations, respectively, as indicated by the two blue bars in the upper panel of Fig. 8.

Turning attention to the optimal MRF structures, it is seen in the upper subplots of Fig. 8 that the optimally designed modular system always requires the largest self-weights in achieving the target frequencies, whereas the MRF with rigid connections always has the smallest self-weights. Specifically, for the first-mode optimisation (upper left subplot), the optimal MRFs with semi-rigid and rigid connections achieve the target frequency of 0.937 Hz with a self-weight of 7323.3 kg and 6777.0 kg, respectively. These values are 5.9% and 12.9% lighter than the self-weight of the corresponding optimal modular system, respectively. For the second-mode optimisation in the global x-direction (upper right subplot), the optimal MRF structures with two different connection stiffnesses achieve the target frequency of 1.023 Hz with a self-weight of 6837.7 kg and 6333.3 kg, respectively. These values are 13.6% and 20.0% lighter than the self-weight of the corresponding optimal modular system, respectively. The above finding suggests that, within an optimal/minimum-weight design setting, the conventional MRF system tend to be more efficient than the unbraced modular system in achieving

a particular natural frequency. This finding is attributed to two facts. First, the vertical and horizontal joint beams in the modular system are released for bending such that adjacent intra-connection joints can undergo different rotations and vertical displacements in resisting lateral loads, as can be seen in the zoomed-in views in Figs. 7(a) and (b), respectively. Accordingly, the modular system in Fig. 6(a) behaves like three separate one-bay MRFs that are constrained (by tie plates) to share the same horizontal displacements in the global-x and global-y directions. By replacing the horizontal and vertical joint beams in Fig. 6(a) with rigid link elements, the fundamental and second natural frequencies of the initial modular system in Table 3 are increased by 5.5% and 10.1%, respectively. Secondly, by allowing independent rotations/displacements at adjacent intra-connection joints, the MBS degenerates to a discontinued MRF with weakened frame members that have smaller flexural rigidities than those of the optimal MRF structure. This argument can be verified by cross comparing the optimal sections reported in Table 4 for the modular system and in Table 5 for the semi-rigid MRF. Indeed, in the optimal modular design, the floor and ceiling beams in the same storey are roughly of the same size with similar second moment of inertia about the major axis, which is not the case in the initial design in Table 3.Incidently, in many previous studies, deeper RHS sections are used for floor beams due to larger gravitational loads on the floor deck, while smaller SHS sections are used for ceiling beams due to decreased loads (cf., [50,55,61]). Nevertheless, it is revealed here, through SO, that the ceiling beams are also important for increasing the lateral stiffness of unbraced modular buildings. At this junction, it should be pointed out that although the MRF benchmark structure requires less structural steel in meeting a particular frequency, the achievement of rigid connection for MRF structures in practice requires an extensive amount of fabrication on-site and, consequently, can be relatively expensive [62]. Furthermore, it should be reemphasised that the rotational stiffness of the so-called semi-rigid connection here corresponds to the classification boundary between the “rigid” and “semi-rigid” connections for unbraced MRFs in Eurocode 3. In this context, the material-saving percentages in Fig. 8 for “semi-rigid” MRF are more realistic than those based on the perfectly rigid connection assumption.

Finally, for natural frequencies of optimally designed structures, it is seen in the lower subplots of Fig. 8 that all optimal designs are able to satisfy their corresponding frequency constraints successfully, in the sense that the normalised heights of all bars are above 1.000. The frequency of optimised structural systems usually need to exceed but to be as close to the target frequency as possible so that the frequency constraint is satisfied

without much redundancy in the systems. Specifically, in the lower subplots of Fig. 8, all normalised frequencies are smaller than 1.011 across the board. To this end, it can be safely concluded that the mapping strategy proposed in section 2.3 works rather well for both unbraced modular and MRF structures, which are designed to carry the lateral loads mainly through member bending. For braced frame structures, the mapping strategy for bracing elements can be modified conveniently to only consider their cross-sectional areas for mapping. Note, the rounding/mapping operation from continuous to discrete is not as trivial as it seems [63], as it may lead to either a feasible but over-conservative design [64] or an infeasible design [65].

As a final remark, the numerical data and conclusion herein should be taken with caution, as several factors can influence the results, such as outer widths of corner posts and MRF columns assumed in the minimum-weight design process. Another factor is the number of columns/bays of the MRF in the global x-direction: by removing the two central columns in Fig. 6(b), the optimised MRF structure (now with one bay in the global-x direction) becomes even lighter in meeting the first target frequency for the fundamental vibration mode in the global-y direction but *heavier* than the optimal modular structure in satisfying the second frequency constraint on the second mode in the global-x direction. At last, the two structural systems are forced to share the same total additional/imposed gravitational loads in order for the cross-comparison to be meaningful and fair. In reality, however, superimposed loads in the two structures can vary significantly depending on their usage, floor/ceiling system, wall panels/partition walls, cladding, etc. In this regard, innovative structural solutions, such as prefabricated lightweight components using composite materials (cf., [66,67]), cellular/perforated beams with large web openings (cf., [68-72]), composite beams with precast hollow-core slabs (cf., [73]), and fully prefabricated lightweight flooring systems [74-77], can naturally find their application in MBS, with the potential of reducing imposed masses significantly.

Table 4. Optimal sections of the modular building system in figure 6(a) with hinged inter-connection joints. Sizing optimisation is first for the fundamental vibration mode in global y-direction and then for the second vibration mode in global x-direction.

Member group	Optimal sections (for $f_{1,target}$=0.937Hz)	Optimal sections (for $f_{2,target}$=1.023Hz)

Corner posts	1st storey	SHS120/10.0	SHS120/12.5
	2nd storey	SHS120/6.3	SHS120/5.0
	3rd storey	SHS120/5.0	
Ceiling beams	1st storey	RHS180×100/4.0	RHS180×100/4.0
	2nd storey	RHS180×100/4.0	RHS160×80/4.0
	3rd storey	RHS120×60/4.0	RHS100×60/4.0
Floor beams	1st storey	RHS160×80/4.0	RHS160×80/4.0
	2nd storey	RHS160×80/5.0	RHS180×100/4.0
	3rd storey	RHS160×80/4.0	RHS160×80/4.0

Table 5. Optimal sections of the MRF in figure 6(b) with semi-rigid beam-column connections. Sizing optimisation is first for the fundamental vibration mode in global y-direction and then for the second vibration mode in global x-direction.

Member group		Optimal sections (for $f_{1,target}$=0.937Hz)	Optimal sections (for $f_{2,target}$=1.023Hz)
MRF columns	1st storey	SHS160/14.2	SHS160/12.5
	2nd storey	SHS160/8.0	SHS160/10.0
	3rd storey	SHS160/6.3	SHS160/5.0
MRF beams	1st storey	IPE360	IPE330
	2nd storey	IPE330	IPE300
	3rd storey	IPE200	IPE220

5. CONCLUDING REMARKS

The efficacy of an optimality criteria-based minimum-weight design method for modular building systems subjected to a generalised stiffness constraint (stated in natural frequency) has been herein established. This was achieved through an innovative optimisation study involving a three-storey modular building system with

hinged inter-module joints, together with a comparative MRF benchmark structure with two different beam-column connection stiffnesses. The discrete minimum-weight design of the two structures, based on standard steel sections, was obtained through first applying the continuous sizing optimisation algorithm to the structures to find their global optimums and then by rounding the optimums to the nearest, most economical discrete solutions through a one-to-one mapping algorithm. The convergence behaviour and robustness of the sizing algorithm for modular building systems have been numerically verified using a modular testbed model with two different sets of initial cross-sections. Structural efficiency of the modular system (with hinged inter-connection joints) and the comparative MRF (with two different connection stiffnesses) was quantified by cross-comparing the self-weights of optimally designed structures that share similar natural frequencies for the fundamental and second vibration modes separately.

Numerical data demonstrated that the overall lateral stiffness of unbraced modular building systems, measured by natural frequency, is not affected noticeably by the moment release of the bolted inter-module joints considered in this study. It is not until vibration modes 5 and 6 that significant difference in mode shape starts to manifest, meaning that the flexural rigidity of vertical interconnection between upper and lower modules only affects higher modes. More importantly, it was shown that the proposed minimum-weight design method could significantly reduce the self-weight (27.1% and 25.8% lighter for the first and second modes, respectively) of modular building systems while maintaining their overall lateral stiffnesses, depending on how efficient/economical the initial design is. Since the optimality criteria formulation presented herein can be readily adapted to other types of performance constraints (e.g., buckling, displacement, stress), the proposed design method has the potential to be integrated into the design process of modular buildings and modular units for maximising their material utilisation and promoting sustainability. On the other hand, it was found that the semi-rigid MRF with identical outer dimensions and imposed masses can achieve the same target frequencies with smaller self-weights. Within an optimal design setting, the semi-rigid MRF is 13.6% and 5.9% lighter than the modular system (with hinged inter-connection joints) in meeting the first and second target frequencies, respectively. This result was attributed to two facts. First, the end release of inter-connection joints makes the modular system behave like a discontinued MRF such that adjacent intra-connection joints can develop different rotations and displacements under lateral loads, hence undermining the double-beam and double-column effects. Second, by cross-comparing optimal sections of two structural systems, the sizing algorithm seemed to equally

redistribute the material between the ceiling beams and floor beams in the same storey of the modular building system, making the optimal beam sections less stiff (bending wise) than those used in the optimally designed MRF.

As a closing note, it is envisaged that the structural optimisation tools and numerical results furnished in this study will serve as a valuable first stepping stone towards achieving resilient, sustainable, and economic modular tall buildings. Based on the current study, future research endeavours are expected and welcomed in the following three areas. First, the proposed design method may be applied to realistic modular buildings of different heights with initial geometric and physical (e.g., residual stresses) imperfections considered to systematically investigate their material efficiency (at the structure level) vis-à-vis conventional building structural systems. These advanced modelling features are excluded in the current study as the finite element analysis in this work is limited to linear elastic modal analysis only, while global and local instability behaviours of modular building systems, which are more susceptible to the above imperfections, fall outside of the scope of work. Second, given the information here, a smart inter-connection joint, which enables easy deconstruction and reuse while having adequate rigidity and resistance, is to be devised so that efficacy of the proposed optimisation method can be further improved with even larger steel savings. In developing such a joint, sizing optimisation techniques may be employed again to determine optimal values of certain design parameters of the inter-module joint. At last, a more comprehensive optimisation strategy, which takes into account manufacturability of modular units and buildability of modular building systems, is warranted to help design engineers reduce overall costs and improve schedule certainty of modular building systems.

APPENDIX - A

For demonstrating correctness of the proposed sizing design method, a planar MRF shown in Fig. A.1(a) is adopted as the testbed structure with a frequency constraint imposed on its fundamental vibration mode. The structure comprises one IPE beam and two SHS columns of the same section. The SO problem here involves determining optimal cross-sectional areas of the MRF's columns, a_1, and beam, a_2, to increase its fundamental frequency, $f_1(a_1,a_2)$, by 100% while requiring minimum amount of steel. For illustrative purpose, the two DVs are bounded by the side constraint [$1.0\mathbf{a_o}$, $3.0\mathbf{a_o}$], where $\mathbf{a_o}$ is a vector collecting initial, non-optimal cross-

sectional areas of the MRF, i.e., $\mathbf{a_o} = [a_{1,o}, a_{2,o}]$. The demonstration is done numerically at two levels. Firstly, the continuous-valued sizing algorithm in Section 2.2 is applied to find optimal cross-sectional areas of the beam and columns; then, the numerically determined optimal DVs are verified against the theoretical optimal values, found by a graphical method. Next, the mapping algorithm in Section 2.3 is employed to convert the continuous-valued optimal solution to standard steel sections; the latter are then compared with optimal standard sections found via combinatorial/exhaustive search.

In pursuit of the first aim, the SO problem is solved graphically using MATLAB® in the continuous design space to find the theoretical optimum, as shown in Figs. A.1 (a) and (b). Specifically, Fig. A.1 (a) plots the fundamental frequency surface $f_1(\mathbf{a})$ of the MRF and target frequency plane $f_{1,target}$ in the normalised a_1-a_2-$f_1(a_1,a_2)$ performance space; both surfaces are normalised by the fundamental frequency of initial MRF, $f_{1,o}$, such that $f_1(a_{1,o}, a_{2,o}) = 1.0$ and $f_{1,target} = 2.0$, while two DVs are normalised by the corresponding values of $\mathbf{a_o}$, respectively. As shown in Fig. A.1 (a), the two normalised surfaces intersect at the red dotted curve, which characterises the frequency constraint for the two DVs to satisfy. This constraint/curve is then projected onto the normalised OF surface $M(\mathbf{a})$ (also by self-weight of the initial MRF) in the normalised a_1-a_2-$M(a_1,a_2)$ design space as shown in Fig. A.1(b) to form another red dotted curve. Evidently, the lowest point on this curve (highlighted by the red dot) corresponds to the minimum-weight design being graphically sought. Normalised optimal values of DVs of this minimum-weight design are summarised in Table A.1 under the name "Theoretical", which reveals that the two DVs need to increase to $[2.190a_{1,o}, 1.160a_{2,o}]$ respectively for the MRF to see the specified increase in the fundamental frequency. Accordingly, the self-weight required for this increase is about 67.0% of the initial design, i.e., $M(\mathbf{a}^*)=1.670M(\mathbf{a_o})$. For verification, optimal values of the same DVs are numerically determined using the sizing algorithm in Section 2.2 and summarised in Table A.1 under the name "Numerical", with the percentage errors (between the numerical and theoretical optimums) reported in the rightmost column. As seen, errors for the two DVs are within +/-3.0%, resulting in a near-optimal solution that is only 0.6% heavier than the theoretical optimum. Moreover, the above sizing optimisation process is fully visualised/traced in Fig. A.1 (b) by the black dash-dotted line, with the arrows indicating moving directions of the current design in the design space as the sizing algorithm iterates. As shown, the sizing process starts at coordinates (1, 1, 1) or green point where the initial MRF is located (due to the above normalisation), and converges successfully at the theoretical optimum or red point after 48 iterations. To shed further light into the convergence behaviour, variations of the

MRF's fundamental frequency throughout the sizing iteration, obtained by the proposed sizing algorithm and the conventional OC method (cf., [38]), are plotted in Fig. A.1(c). As shown, the proposed continuous sizing method converges successfully after 48 iterations, whereas the conventional method fails to converge to the optimum even after 180 iterative steps.

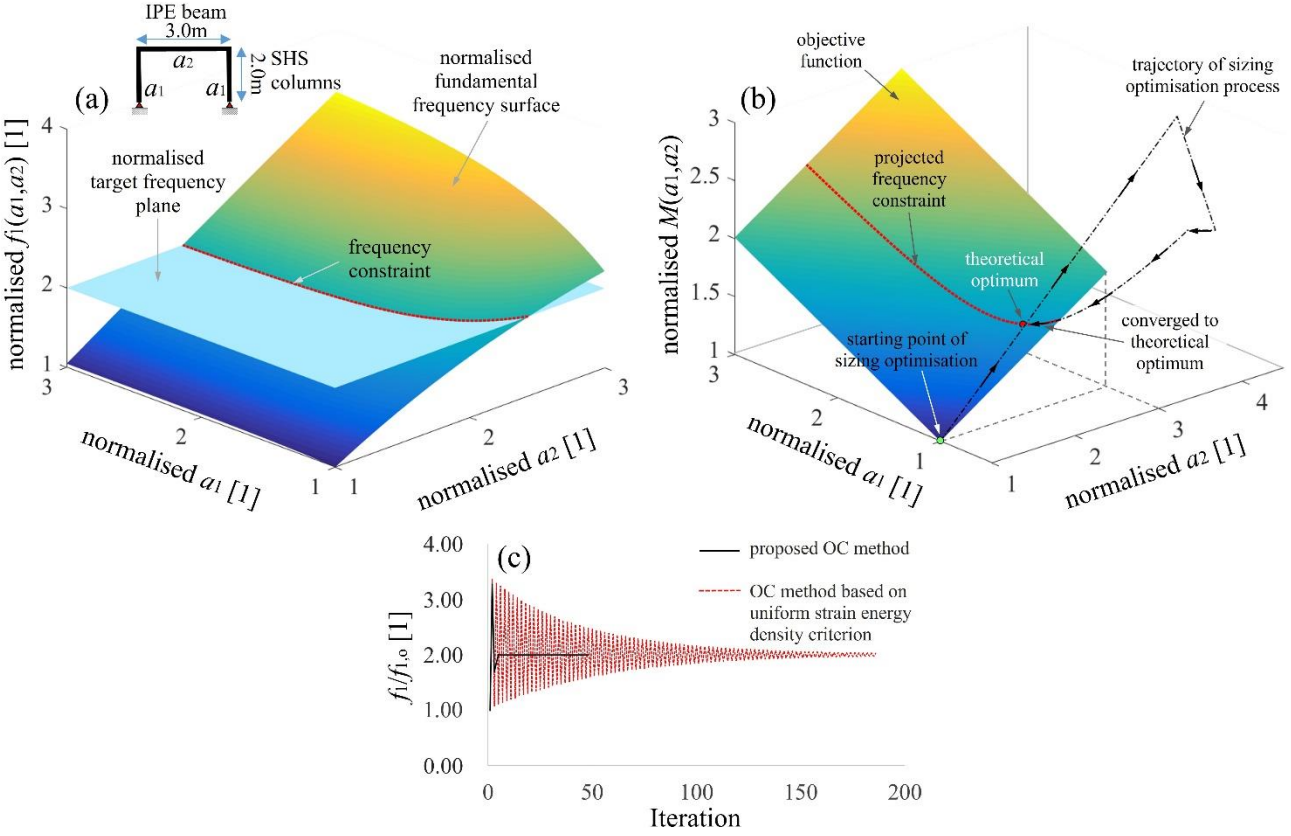

Fig. A.1 (a) fundamental frequency surface of the planar MRF and target frequency plane; (b) theoretical optimum versus numerical optimum found by the proposed sizing optimisation method; and (c) variation histories of the MRF's fundamental frequency during sizing iterations obtained by the proposed OC method and conventional OC method, all values normalised by the corresponding values of the initial (non-optimal) MRF.

Table A.1 Theoretical and numerical optimal values of DVs of the MRF under a frequency constraint on the fundamental vibration mode, quantities normalised by the corresponding values of the initial MRF.

	Continuous-valued optimal solutions

	Theoretical	Numerical	Percentage error
$a_1^* / a_{1,o}$	2.190	2.223	+1.51%
$a_2^* / a_{2,o}$	1.160	1.130	-2.59%
$f_1(\mathbf{a}^*) / f_{1,o}$	2.000	2.000	0.00%
$M(\mathbf{a}^*) / M(\mathbf{a}_o^*)$	1.670	1.671	+0.06%

To the second aim, optimal sectional properties found by the sizing algorithm are used to select standard sections for the MRF following the same mapping strategy in Section 2.3. Sections computed by the proposed discrete design method (see Section 2.3) entail IPE120 profile for the beam and SHS120/5 profile for two columns as in Table A.2. In parallel, a combinatorial search, which includes 1908 combinations of design to evaluate in total (coming from 18 IPE profiles and 106 SHS profiles), is conducted in the discrete design space to determine the absolute optimal standard sections. As shown in the leftmost column in Table A.2, the optimal sections for the beam and columns from the combinatorial search are IPE140 and SHS100/5, respectively. To this end, the discrete design method is unable to find the absolute optimum but instead yields a sub-optimal design. However, the difference in self-weights between the two remains practically small, as the latter is only 5.13% heavier than the former. More importantly, it should be recognised that the absolute optimum is seldom achieved in practice by any numerical optimisation method [39,40], except those found by exhaustive search, which are computationally extremely expensive to retrieve for even moderate-sized SO problems. Overall, pertinent numerical results furnished herein demonstrate correctness of the proposed optimisation techniques for solving continuous- and/or discrete-valued SO problems subjected to natural frequency constraint.

Table A.2 Optimal standard sections of the MRF found by the exhaustive search method and the proposed discrete design method.

	Discrete-valued optimal solutions		
	by combinatorial search method	by proposed discrete design method	Percentage error
Columns' section	SHS100/5	SHS120/5	N/A

Beam's section	IPE140	IPE120	
$f_1 / f_{1,o}$	2.016	2.150	
Self-weight [kg]	97.5	102.5	+5.13%

APPENDIX - B

Herein, the optimality criteria in section 2.1 and sizing algorithm in section 2.2 are extended from a single frequency constraint to multiple constraints. To this end, the sizing optimisation problem, now subjected to r inequality frequency constraints, is expressed as:

$$\begin{aligned} &\mathbf{a}^{*} = \underset{\mathbf{a}^{\min} \le \mathbf{a} \le \mathbf{a}^{\max}}{\arg\min} \left\{ M(\mathbf{a}) = \sum_{i=1}^{n} \rho_i l_i a_i \right\} \\ &\text{s.t. } f_k(\mathbf{a}) - f_{k,\text{target}} \ge 0 \ (k = 1, ..., r) \end{aligned} \tag{A.1}$$

A precondition behind Eq. (A.1) is that the number of active behavioural constraints is smaller than the number of active DVs, i.e., $r < n$, as is typically the case in structural design. In this setting, the Lagrangian function, $L(\mathbf{a}, \boldsymbol{\lambda})$: $\mathbb{R}^n \times \mathbb{R}^r \rightarrow \mathbb{R}$, adjoining r behavioural constraint to the linear objective function, is formed as:

$$L(\mathbf{a}, \lambda) = M(\mathbf{a}) - \sum_{k=1}^{r} \lambda_k \left[f_k(\mathbf{a}) - f_{k,\text{target}} \right], \tag{A.2}$$

where $\boldsymbol{\lambda} \in \mathbb{R}^{r \times 1}$ is a vector collecting r multipliers for r frequency constraints. Assuming differentiability of $f_k(\mathbf{a})$ (k=1,…,r) on the feasible solution set of the OP, the stationary condition of the Lagrangian in Eq. (A.2) with respect to active DVs, i.e., $\nabla_{\mathbf{a}} L(\mathbf{a}, \boldsymbol{\lambda})=0$, yields the following equation:

$$\sum_{k=1}^{r} \frac{\lambda_k}{\rho_j l_j} \frac{\partial f_k(\mathbf{a})}{\partial a_j} = 1 \ (j = 1, ..., n). \tag{A.3}$$

which defines the generalised OC for the sizing OP in Eq. (A.1) in terms of n differential equations. Further, the stationary condition of the Lagrangian in Eq. (A.2) with respect to the multipliers, $\nabla_{\boldsymbol{\lambda}} L(\mathbf{a}, \boldsymbol{\lambda})=\mathbf{0}$, leads back to the r behavioural constraints in Eq. (A.1), i.e.,

$$f_k(\mathbf{a}) - f_{k,\text{target}} = 0 \ (k=1,...,r), \tag{A.4}$$

which are independent of the multipliers. Therefore, Eqs. (A.3) and (A.4) define a system of $n+r$ coupled equations for $n+r$ unknowns, i.e., n DVs plus r multipliers. The original formula for updating the DVs (see Eq. (6)) is modified accordingly based on the new OC in Eq. (A.3) and attains the following form:

$$a_i^{(p+1)} = a_i^{(p)} \left\{ 1 + \frac{1}{\eta} \left[\sum_{k=1}^{r} \frac{\lambda_k^{(p)}}{\rho_i l_i} \left(\frac{\partial f_k(\mathbf{a})}{\partial a_i} \right)^{(p)} - 1 \right] \right\}, \tag{A.5}$$

Upon substituting Eq. (A.5) into Eq. (7) for $k = 1, \ldots, r$, the following equation can be obtained for updating the multipliers at iteration p:

$$\boldsymbol{\lambda}^{(p)} = \left(\mathbf{A}^{(p)} \right)^{-1} \mathbf{B}^{-1}, \tag{A.6}$$

in which the superscript "-1" denotes matrix inversion, and $\mathbf{A}^{(p)} \in \mathbb{R}^{r\times r}$ and $\mathbf{B}^{(p)} \in \mathbb{R}^{r\times 1}$ are given by

$$\mathbf{A}_{r\times r}^{(p)} = \sum_{i=1}^{n} \frac{1}{l_i \rho_i} \left(a_i \frac{\partial (\mathbf{f}^{\mathrm{T}})}{\partial a_i} \frac{\partial \mathbf{f}}{\partial a_i} \right)^{(p)}, \tag{A.7}$$

and

$$\mathbf{B}_{r\times 1}^{(p)}[k,1] = \sum_{i=1}^{n} \left(\frac{\partial f_k}{\partial a_i} a_i \right)^{(p)} + \eta [\, f_{k,\text{target}} - f_k^{(p)}], \tag{A.8}$$

respectively. In Eq. (A.7), $\mathbf{f}^{(p)} \in \mathbb{R}^{1\times r}$ is a row vector collecting the r natural frequencies of the structure at iteration p, i.e., $\mathbf{f}^{(p)} = [f_1, f_2, \ldots, f_r]^{(p)}$, and the superscript "$T$" denotes the transpose of a vector. Clearly, by decreasing the number of behavioural constraints from multiple to single, Eqs. (A.5) for updating the DVs and (A.6) for updating the Lagrangian multipliers degenerate to Eqs. (6) and (8), respectively. At this point, it needs to be pointed out that the above formulation inherently assumes that all r frequency constraints are active/binding simultaneously, i.e., $f_k(\mathbf{a}) - f_{k,\text{target}} = 0$ (k=1,…,r). In reality, however, not all behavioural constraints are binding at the same time so that there is a need to separate active constraints from inactive ones at every iteration p. Further, during the resizing process, only active constraints and their corresponding multipliers are taken into account when using Eqs. (A.5) and (A.6) for updating the DVs and the multipliers, respectively. To this aim, the active (behavioural) constraint set can be estimated through a so-called constraint thickness parameter, $t^{(p)}$, that defines a gradually tightened finite interval $[-t^{(p)}, 0]$ within which all constraints are considered active. This thickness interval can be evaluated by the following equation according to Patnaik et al. [39]:

$$t^{(p)} = \tau^{(p-1)} t_0, \tag{A.9}$$

where $t^{(p)}$ is the constraint thickness at iteration p, t_0 is the initial constraint thickness, and $\tau \in (0,1)$ is a factor by which the constraint thickness is tightened at each iteration.

REFERENCES

[1] UNEP. Global Status Report 2017. United Nations Environment Programme 2017.

[2] IEA - International Energy Agency. World Energy Balances. International Energy Agency 2017.

[3] Ferdous W, Bai Y, Ngo T, Manalo A, Mendis P. New advancements, challenges and opportunities of multi-storey modular buildings - a state-of-the-art review. Eng Struct 2019; 183: 883–893.

[4] Allwood JM, Ashby MF, Gotwski TG, Worrel E. Material efficiency: a white paper. Resour Conserv

Recycl 2011; 55(3): 362–381.

[5] Orr J, Drewnioka MP, Walkerb I, Ibellc T, Coppingc A, Emmitt S. Minimising energy in construction: Practitioners' views on material efficiency. Resour Conserv Recycl 2019; 140(2019): 125-136.

[6] Iacovidou E, Purnell P, Tsavdaridis KD, Poologanathan K. Digitally Enabled Modular Construction for Promoting Modular Components Reuse: A UK View. J Build Eng 2021; https://doi.org/10.1016/j.jobe.2021.102820.

[7] Generalova E, Generalov V, Kuznetsova A. Modular buildings in modern construction. Procedia Eng 2016; 153(2016): 167–172.

[8] O'Neill D, Organ S. A literature review of the evolution of British prefabricated low-rise housing. Struct Surv 2016; 34: 191–214.

[9] Lacey AW, Chen W, Hao H, Bi K. Structural Response of Modular Buildings – An Overview. J Build Eng 2018; https://doi.org/10.1016/j.jobe.2017.12.008.

[10] Liew JYR, Chua YS, Dai Z. Steel concrete composite systems for modular construction of high-rise buildings. Structures 2019; 21: 135–49.

[11] Navaratnam S, Ngo T, Gunawardena T, Henderson D. Performance review of prefabricated building systems and future research in Australia. Buildings 2019; 9(2): 38.

[12] Li ZY, Tsavdaridis KD, Gardner L. A Review of Optimised Additively Manufactured Steel Connections for Modular Building Systems. Proc of International Conference on Additive Manufacturing in Products and Applications 2020; Zurich: Springer, Cham; 357-373.

[13] Lawson RM, Ogden RG, Bergin R. Application of modular construction in highrise buildings. J Archit Eng 2012; 18: 148 - 154.

[14] Mills S, Grove D, Egan M. Breaking The Pre-fabricated Ceiling: Challenging the Limits for Modular High-Rise. Proc of the CTBUH International Conference 2015. NY: Council on Tall Buildings and Urban Habitat, Chicago; 416-425.

[15] Lacey AW, Chen W, Hao H, Bi K. Review of bolted inter-module connections in modular steel buildings. J Build Eng 2019; 23, 207-219.

[16] Lacey AW, Chen W, Hao H, Bi K, Tallowin FJ. Shear behaviour of post-tensioned inter-module connection for modular steel buildings. J Constr Steel Res 2019; 162, 105707.

[17] Lacey AW, Chen W, Hao H, Bi K. New interlocking inter-module connection for modular steel buildings: Simplified structural behaviours. Eng Struct 2021; 227, 111409.

[18] Srisangeerthanan S, Hashemi MJ, Rajeev P, Gad E, Fernando S. Review of performance requirements for inter-module connections in multi-story modular buildings. J Build Eng 2020; 28, 101087.

[19] Sendanayake SV, Thambiratnam DP, Perera N, Chan T, Aghdamy S. Seismic mitigation of steel modular building structures through innovative inter-modular connections. Heliyon 2019; 5(11), e02751.

[20] Sendanayake SV, Thambiratnam DP, Perera N, Chan T, Aghdamy S. Enhancing the lateral performance of modular buildings through innovative inter-modular connections. Structures 2021; 29, 167-184.

[21] Gatheeshgar P, Poologanathan K, Gunalan S, Tsavdaridis KD, Nagaratnam B, Iacovidou E. Optimised cold-formed steel beams in modular building applications. J Build Eng 2020; 32(2020): 101607.

[22] Chan CM, Grierson DE, Sherbourne AN. Automatic optimal design of tall steel building frameworks. J Struct Eng 1995; 121(5), 838-847.

[23] Chan CM, Chui JKL. Wind-induced response and serviceability design optimisation of tall steel buildings. Eng Struct 2006; 28, 503-513.

[24] Spence SMJ, Kareem A. Data-Enabled Design and Optimization (DEDOpt): Tall steel building frameworks. Comput Struct 2013; 129, 134-147.

[25] Spence SMJ. Optimization of uncertain and dynamic high-rise structures for occupant comfort: An adaptive kriging approach. Struct Saf 2018; 75, 57-66.

[26] Petrini F, Giaralis A, Wang Z. Optimal tuned mass-damper-inerter (TMDI) design in wind-excited tall buildings for occupants' comfort serviceability performance and energy harvesting. Eng Struct 2020; 204: 109904.

[27] Ruiz R, Taflanidis AA, Giaralis A, Lopez-Garcia D. Risk-informed optimization of the tuned mass-damper-inerter (TMDI) for the seismic protection of multi-storey building structures. Eng Struct 2018; 177: 836-850.

[28] Wang Z, Giaralis A. Top-storey softening for enhanced mitigation of vortex shedding induced vibrations in wind-excited optimal tuned mass damper inerter (TMDI)- equipped tall buildings. J Struct Eng 2020; DOI: 10.1061/(ASCE)ST.1943- 541X.0002838.

[29] Wang Z, Giaralis A. Enhanced motion control performance of the tuned massdamper inerter through

primary structure shaping. Struct Control Health Monit 2021; e2756. DOI: 10.1002/stc.2756.

[30] Jing J, Clifton C, Roy K, Lim J. Three-storey modular steel building with a novel slider device: Shake table tests on a scaled down model and numerical investigation. Thin Wall Struct 2020; 155(2020), 106932.

[31] Jing J, Clifton C, Roy K, Lim J. Performance of a novel slider device in multi-storey cold-formed steel modular buildings under seismic loading. Structures 2020; 27(2020), 212-246.

[32] Jing J, Clifton C, Roy K, Lim J. Seismic protection of modular buildings with bonded rubber unit sliders: Experimental study. Thin Wall Struct 2020; 154(2020), 106790.

[33] Jing J, Clifton C, Roy K, Lim J. Seismic protection of modular buildings with galvanised steel wall tracks and bonded rubber units: Experimental and numerical study. Thin Wall Struct 2021; 162(2021), 107563.

[34] Gatheeshgar P, Dobson R, Poologanathan K, Tsavdaridis KD, Nagaratnam B, Iacovidou E. Modular building design: post-brexit housing. Proc 14th Nordic Steel Construction Conference 2019. Copenhagen, Denmark.

[35] Khot NS. Nonlinear analysis of optimized structure with constraints on system stability. AIAA Journal 1983; 21(8), 1181-1186.

[36] Levy R. Optimal design of trusses for overall stability. Comput Struct 1994; 53(5), 1133-1138.

[37] Rubin CP. Minimum weight design of complex structures subject to a frequency constraint. AIAA Journal 1970; 8(5), 923.

[38] Venkayya VB. Design of optimum structures. Comput Struct 1971; (1): 265 – 309.

[39] Patnaik SN, Guptill JD, Berke L. Merits and limitations of optimality criteria method for structural optimization. Int J Numer Meth Eng 1995; (38)18: 3087-3120.

[40] Kirsch U. Structural Optimization Fundamentals and Applications. Springer-Verlag Berlin Heidelberg; 1993.

[41] Lógó J. New Type of Optimal Topologies by Iterative Method. Mech Based Des Struct Mach 2005; 33(2): 149-171.

[42] Venkayya VB. Optimality criteria: A basis for multidisciplinary design optimization. Comput Mech 1989; 5(1):1-21.

[43] Svanberg K. On local and global minima in structural optimization. New Directions in Optimum Structural Design 1984. NY: Wiley; 327–341.

[44] Christensen P, Klarbring A. An introduction to structural optimization. Springer Netherlands; 2019.

[45] Berke L, Khot NS. Use of optimality criteria approach to structural optimization for large scale systems. Structural Optimization, AGARD LS-70, 1974; 1-29.

[46] Berke L, Khot NS. Structural Optimization Using Optimality Criteria. Proc NATO Advanced Study Institute on Computer Aided Optimal Design: Structural and Mechanical Systems 1987; Tróia, Portugal: Springer-Verlag.

[47] Wittrick WH. Rates of Change of Eigenvalues, With Reference to Buckling and Vibration Problems. The Aeronautical Journal 1962; 66(621): 590-591.

[48] Allwood RJ, Chung YS. Minimum-weight design of trusses by an optimality criteria method. Int J Numer Methods Eng 1984; 20: 697–713.

[49] Khot NS, Berke L, Venkayya VB. Comparison of optimality criteria algorithms for minimum weight design of structures. AIAA Journal 1979; 17(2): 182-190.

[50] Dhanapala J, Ghaedniaa H, Dasa S, Velocci J. Structural performance of state-of-the-art VectorBloc modular connector under axial loads. Eng Struct 2019; 183: 496-509.

[51] Chua YS, Liew JYR, Pang SD. Robustness of prefabricated prefinished volumetric construction (PPVC) high-rise building. Proceedings of the 12th international conference on Advances in Steel-Concrete Composite Structures (ASCCS 2018); 913–919.

[52] Gunawardena T, Ngo T, Mendis P. Behaviour of multi-storey prefabricated modular buildings under seismic loads. Earthq Struct 2016; 11(6): 1061-1076.

[53] Sultana P, Youssef MA. Seismic performance of modular steel-braced frames utilizing superelastic shape memory alloy bolts in the vertical module connections. J Earthq Eng 2018; 2018:1–25.

[54] Shan S, Pan W. Structural design of high-rise buildings using steel-framed modules: A case study in Hong Kong. Struct Design Tall Spec Build 2020; 29:e1788.

[55] Shi F, Wang H, Zong L, Ding Y, Su J. Seismic behavior of high-rise modular steel constructions with various module layouts. J Build Eng 2020, 31: 10396.

[56] Thai HT, Ngo T, Uy B. A review on modular construction for high-rise buildings. Structures 2020; 28: 1265-1290.

[57] Annan CD, Youssef MA, El Naggar MH. Experimental evaluation of the seismic performance of modular

steel-braced frames. Eng Struct 2009; 31:1435–46.

[58] Brincker R, Ventura CE. Introduction to Operational Modal Analysis. John Wiley & Sons Ltd; 2015.

[59] Lacey AW, Chen W, Hao H, Bi K. Effect of inter-module connection stiffness on structural response of a modular steel building subjected to wind and earthquake load. Eng Struct 2020; 213: 110628.

[60] Chan CM. An optimality criteria algorithm for tall buildings design using commercial standard sections. Journal of Structural Optimization 1992; 5: 26–29.

[61] Peng J, Hou C, Shen L. Lateral resistance of multi-story modular buildings using tenon connected inter-module connections. J Constr Steel Res 2020; 177: 106453.

[62] De Alvarenga AR. Plastic-zone advanced analysis – Formulation including semi-rigid connection. Eng Struct 2020; 212: 110435.

[63] Schevenels M, McGinn S, Rolvink A, Coenders J. An optimality criteria-based method for discrete design optimization under buildability constraints. Struct Multidisc Optim 2014; 50: 755–774.

[64] Templeman A. Discrete optimum structural design. Comput Struct 1988; 30(3): 511-518.

[65] Arora J, Huang M, Hsieh C. Methods for optimisation of nonlinear problems with discrete variables: a review. Struct Multidiscip Optim 1994; 8(2): 69-95.

[66] Manalo A. Structural behaviour of a prefabricated composite wall system made from rigid polyurethane foam and Magnesium Oxide board. Constr Build Mater 2013; 41: 642-53.

[67] Satasivam S, Bai Y, Zhao XL. Adhesively bonded modular GFRP web–flange sandwich for building floor construction. Compos Struct 2014; 111: 381-392.

[68] Tsavdaridis KD, D'Mello C. FE Investigation of Perforated Sections with Standard and Non-Standard Web Opening Configurations and Sizes. Proc of 6th International Conference on Advances is Steel Structures 2009; Hong Kong: ICASS09 Press: 213-220.

[69] Tsavdaridis KD, D'Mello C, Hawes M. Experimental Study of Ultra Shallow Floor Beams (USFB) with Perforated Steel Sections. Proc 11th Nordic Steel Construction Conference 2009; Malmö, Sweden; 128: 312-319.

[70] Tsavdaridis KD, D'Mello C. Optimisation of Novel Elliptically-Based Web Opening Shapes of Perforated Steel Beams. J Constr Steel Res 2012; 76, 39-53.

[71] Rajana K, Tsavdaridis KD, Koltsakis E. Elastic and Inelastic Buckling of Steel Cellular Beams under

Strong-Axis Bending. Thin Wall Struct 2020; 156(1-3): 106955.

[72] Tsavdaridis KD, Lau CK, Rodríguez AA, Experimental behaviour of non-seismical RWS connections with perforated beams under cyclic actions. J Constr Steel Res 2021; 183(4):106756.

[73] Ferreira FPV, Tsavdaridis KD, Martins CH, De Nardin S. Steel–Concrete-Composite Beams with Precast Hollow-Core Slabs: A Sustainable Solution. Sustainability 2021; 13: 4230.

[74] Ahmed IM, Tsavdaridis KD . Life Cycle Assessment (LCA) Study of European Lightweight Composite Flooring Systems. J Build Eng 2018; 20: 624-633.

[75] Ahmed IM, Tsavdaridis KD . The Evolution of Composite Flooring Systems: Applications, Testing, Modelling and Eurocode Design Approaches. J Constr Steel Res 2019; 155; 286-300.

[76] Ahmed IM, Tsavdaridis KD. Shear Connection of Prefabricated Slabs with Lightweight Concrete - Part 1: Experimental and Analytical Work. J Constr Steel Res 2020; 169: 106016.

[77] Gatheeshgar P, Poologanathan K, Thamboo J, Roy K, Rossi B, Molkens T, Perera D, Navaratnam S. On the fire behaviour of modular floors designed with optimised cold-formed steel joists. Structures 2021; 30: 1071-1085.